

# **SANDIA REPORT**

SAND2012-3369  
Unlimited Release  
Printed May 2012

## **Basics of Polar-Format Algorithm for Processing Synthetic Aperture Radar Images**

Armin W. Doerry

Prepared by  
Sandia National Laboratories  
Albuquerque, New Mexico 87185 and Livermore, California 94550

Sandia National Laboratories is a multi-program laboratory managed and operated by Sandia Corporation, a wholly owned subsidiary of Lockheed Martin Corporation, for the U.S. Department of Energy's National Nuclear Security Administration under contract DE-AC04-94AL85000.

Approved for public release; further dissemination unlimited.



**Sandia National Laboratories**

Issued by Sandia National Laboratories, operated for the United States Department of Energy by Sandia Corporation.

**NOTICE:** This report was prepared as an account of work sponsored by an agency of the United States Government. Neither the United States Government, nor any agency thereof, nor any of their employees, nor any of their contractors, subcontractors, or their employees, make any warranty, express or implied, or assume any legal liability or responsibility for the accuracy, completeness, or usefulness of any information, apparatus, product, or process disclosed, or represent that its use would not infringe privately owned rights. Reference herein to any specific commercial product, process, or service by trade name, trademark, manufacturer, or otherwise, does not necessarily constitute or imply its endorsement, recommendation, or favoring by the United States Government, any agency thereof, or any of their contractors or subcontractors. The views and opinions expressed herein do not necessarily state or reflect those of the United States Government, any agency thereof, or any of their contractors.

Printed in the United States of America. This report has been reproduced directly from the best available copy.

Available to DOE and DOE contractors from

U.S. Department of Energy  
Office of Scientific and Technical Information  
P.O. Box 62  
Oak Ridge, TN 37831

Telephone: (865) 576-8401  
Facsimile: (865) 576-5728  
E-Mail: [reports@adonis.osti.gov](mailto:reports@adonis.osti.gov)  
Online ordering: <http://www.osti.gov/bridge>

Available to the public from

U.S. Department of Commerce  
National Technical Information Service  
5285 Port Royal Rd.  
Springfield, VA 22161

Telephone: (800) 553-6847  
Facsimile: (703) 605-6900  
E-Mail: [orders@ntis.fedworld.gov](mailto:orders@ntis.fedworld.gov)  
Online order: <http://www.ntis.gov/help/ordermethods.asp?loc=7-4-0#online>



SAND2012-3369  
Unlimited Release  
Printed May 2012

# **Basics of Polar-Format Algorithm for Processing Synthetic Aperture Radar Images**

Armin Doerry  
ISR Mission Engineering

Sandia National Laboratories  
PO Box 5800  
Albuquerque, NM 87185-0519

## **Abstract**

The purpose of this report is to provide a background to Synthetic Aperture Radar (SAR) image formation using the Polar Format (PFA) processing algorithm.

This is meant to be an aid to those tasked to implement real-time image formation using the Polar Format processing algorithm.

## **Acknowledgements**

The production of this updated edition report was funded by General Atomics Aeronautical Systems, Inc. (ASI) Reconnaissance Systems Group (RSG).

General Atomics ASI, Inc., builds the high-performance Lynx SAR/GMTI system.

# Contents

Foreword.....	6
1 Introduction .....	7
2 Background.....	9
3 SAR Imaging in a 2-D World.....	15
3.1 General Image Transform .....	20
3.2 Small Aperture Approximations .....	22
3.3 Polar Reformatting .....	23
3.4 Polar Reformatting with Real-time Motion Compensation .....	26
3.5 Polar Reformatting using a Chirped Z-Transform .....	29
3.6 SAR Image Formation .....	32
3.7 Complex Data Interpolation .....	36
4 SAR Imaging in a 3-D World.....	37
4.1 Classical Phase History Data Collection .....	38
4.2 Generalized Data Collection with Real-time Motion Compensation.....	42
4.3 Image Formation using CZT .....	44
5 MATLAB Implementation.....	51
6 Polar Format Processing Extensions .....	53
6.1 Residual Video Phase Error Correction .....	53
6.2 Polar Format Processing with Subapertures.....	54
6.3 Partial Wavefront Curvature Error Correction Between Transforms .....	54
6.4 Wavefront Curvature Correction in Post Processing .....	54
6.5 Autofocus .....	54
6.6 Data Prefiltering .....	55
6.7 Geometric Corrections .....	56
7 Block Diagrams .....	57
8 Point Design Examples.....	61
9 Conclusions .....	63
References.....	65
Distribution .....	66

## Foreword

The Polar Format Algorithm for Synthetic Aperture Radar image formation is well documented in the literature. The precursor to this report was a limited distribution internal Sandia National Laboratories report titled “Real-time Polar-Format Processing for Sandia’s Testbed Radar Systems”, SAND2001-1644P, printed June 2001.

This current report has been edited to remove references to Sandia programs and other limited distribution publications and sources. It is judged that this takes away virtually nothing of the value of the report for the vast majority of readers. In addition, some typographical errors from the first report were fixed along the way.

This report contains no intellectual property outside of the public domain. Its purpose was to summarize and educate, not to reveal any “secret sauce”. This report just fills in a lot of the background that other sources tend to overlook, or otherwise leave to the reader.

# 1 Introduction

There are many ways to view the process of forming an image using Synthetic Aperture radar (SAR) collected data. The various viewpoints illustrate or highlight different aspects of the process and make the certain aspects easier to understand, by perhaps relating them to other more familiar processes. In the end one might ask “Which is the ‘right’ way to look at image formation?” to which the only answer is “They all are.” (Well, not exactly... there are certainly some less-than-right ways that tend to obfuscate things, in spite of their popularity.)

However, insisting that a single right way exists (and especially that it happens to be ‘your’ way) is akin to seeing the world through a green filter, and denying oneself the richness of (or the utility of) experiencing other colors. Unfortunately, this analogy is quite commonly applicable in the radar community, and in fact hampers advancing the state-of-the-art.

This report discusses the Polar Format Algorithm (PFA) for SAR image formation, first described by Walker.<sup>1</sup> A natural question is “Why use PFA processing as opposed to say linear range-Doppler subaperture techniques?” Though the extended answer to this question is beyond the scope of this report, the short answer is simply stated as “Because, as will be shown, the basic collected SAR phase history data is collected in a polar coordinate frame of the frequency space of the image, and if you don’t fix this, you will be limited by it, especially as resolutions approach the nominal wavelength of the SAR.” This is the case for techniques like the Overlapped Subaperture Algorithm (OSA). PFA processing does fix this, and consequently is not so limited by this (although other limitations exist that are not as pertinent at ultra-fine resolutions). An extensive treatment of the relative strengths and weaknesses of various algorithms can be found elsewhere.<sup>2,3,4</sup> This report henceforth deals strictly with PFA processing.

It is suggested that a reader who is inclined to want to fully understand the concepts presented herein, secure pencil and paper and derive for himself the various equations, using this report as a guide. This might allow the reader to ‘fill in’ the missing steps and understand their significance.

*“Get your facts first, then you can distort them as you please.”*  
*-- Mark Twain.*

## 2 Background

### Wavenumbers

For completeness, we begin at the very beginning. There is no intent here to insult anyone's intelligence, but rather to clearly define the framework of ideas for subsequent discussions.

Consider a traveling wave moving in the  $+x$  direction. This can be described as

$$w(t, x) = A \cos(\omega t - kx) \quad (1)$$

where

$$\begin{aligned} t &= \text{time with units seconds} \\ x &= \text{spatial distance with units meters} \\ \omega &= \text{frequency (temporal phase rate) with units radians/second} \\ k &= \text{wavenumber (spatial phase rate) with units radians/meter.} \end{aligned} \quad (2)$$

We identify the phase

$$(\omega t - kx) = \omega \left( t - \frac{k}{\omega} x \right) = \omega \left( t - \frac{1}{c} x \right) = \left( \omega t - \frac{\omega}{c} x \right) \quad (3)$$

where we recognize

$$\begin{aligned} c &= \frac{\omega}{k} = \text{velocity of propagation of the wave in m/s, and furthermore} \\ \lambda &= \frac{2\pi}{k} = \text{wavelength in meters.} \end{aligned} \quad (4)$$

The key point here is that we can (and do) speak of spatial 'frequencies' which are more appropriately called wavenumbers.

“Why is this important?” Because radar imaging, specifically Synthetic Aperture Radar (SAR) imaging, is more about processing wavenumber information than about frequency information. What allows us to use frequency information is that wavenumber and frequency are related by the velocity of propagation that we claim to know (but sometimes really don't, at least with sufficient accuracy and/or precision).

While time seems to have but a single dimension, space has up to three that we know about. The travelling wave equation then becomes (for a planar wave front, i.e. a plane wave)

$$w(t, x, y, z) = A \cos(\omega t - k_x x - k_y y - k_z z) \quad (5)$$

where each dimension has its own wavenumber component. In vector notation we can write this as

$$w(t, \mathbf{r}) = A \cos(\omega t - \mathbf{k} \cdot \mathbf{r}) \quad (6)$$

where

$$\begin{aligned} \mathbf{r} &= \text{a position vector, and} \\ \mathbf{k} &= \text{a wavenumber vector.} \end{aligned} \quad (7)$$

Alternatively, we can write the wavenumber vector in a magnitude-direction sort of format as

$$\mathbf{k} = k \hat{\mathbf{n}} \quad (8)$$

where

$$\begin{aligned} k &= \text{the magnitude of the wavenumber vector, and} \\ \hat{\mathbf{n}} &= \text{a unit vector pointing in the direction that the wave is travelling.} \end{aligned} \quad (9)$$

This allows us to write

$$w(t, \mathbf{r}) = A \cos(\omega t - k \hat{\mathbf{n}} \cdot \mathbf{r}) = A \cos(\omega t - k(\hat{\mathbf{n}} \cdot \mathbf{r})) \quad (10)$$

where we also realize that  $k$  is the wavenumber in the direction that the wave is travelling. Clearly, in the space-time universe we live in, there is but a single frequency, but at least 3 wavenumber components to fully describe a travelling wave. The properties of SAR imaging are governed by this as well.

Consider a two-dimensional universe with a traveling wave consistent with the illustration in Figure 1. We observe the following.

- The lines represent constant phase contours at a snapshot in time.
- The waves are travelling perpendicular to these constant phase contours.
- We recognize that  $\hat{\mathbf{n}} = \hat{\mathbf{x}} \cos \theta + \hat{\mathbf{y}} \sin \theta$  such that we can write

$$k \hat{\mathbf{n}} \cdot \mathbf{r} = (k \cos \theta)x + (k \sin \theta)y. \quad (11)$$

This really describes how the phase information is oriented in the (in this case) universe. We will see this form again.

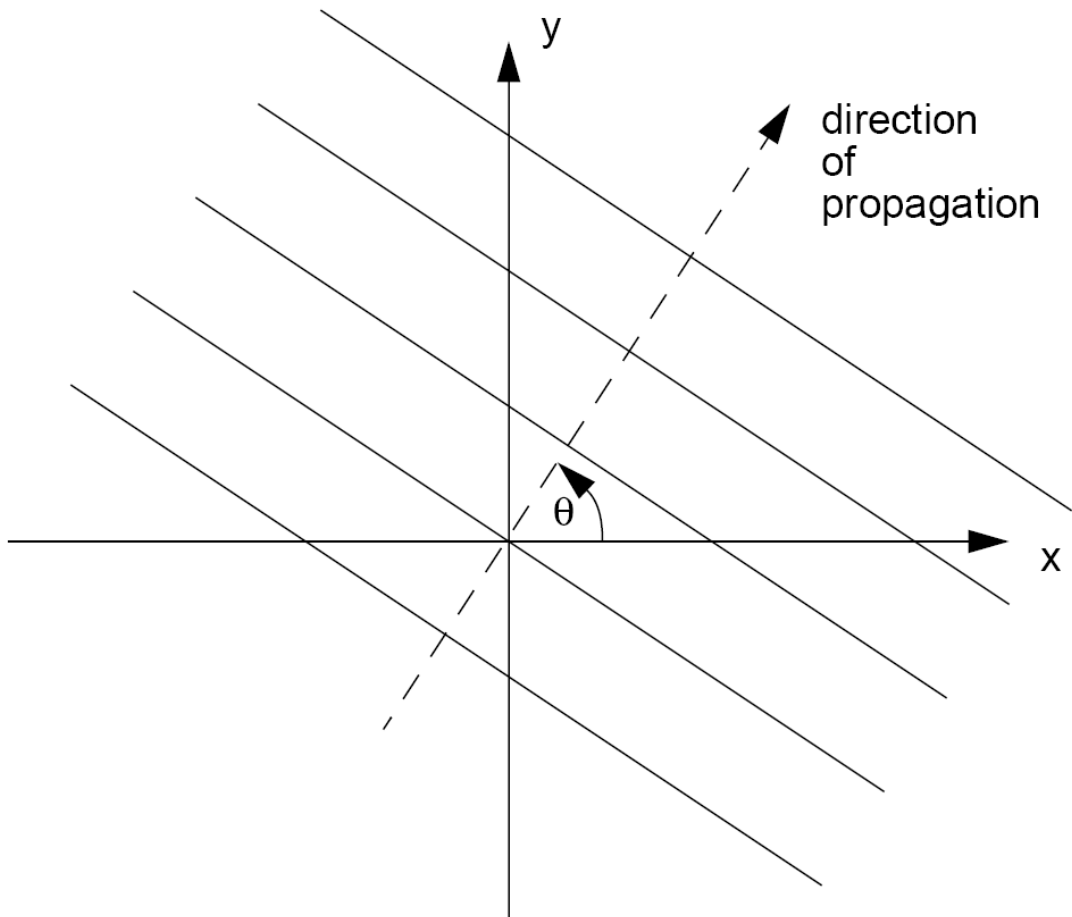


**Figure 1. Illustration of linear wavefronts for a traveling wave in a 2-D geometry.**

Now some more comments about frequency and wavenumber.

Reconsider the 1-Dimensional traveling wave, with phase

$$\Theta = \omega t - kx \quad (12)$$

where  $\omega$  is unknown, and  $k$  and  $x$  are fixed but also unknown, but  $\Theta$  can be measured at known times  $t$ . A single measurement of  $\Theta$  at some time  $t = t_0$  is useless for estimating  $\omega$ , but since we observe that

$$\omega = \frac{d\Theta}{dt} \quad (13)$$

we can estimate  $\omega$  from observing how  $\Theta$  changes over time. The precision of our estimate (i.e. frequency resolution) depends on how long in time we observe  $\Theta$ .

In a similar manner, if the net phase is observed over a variety of frequencies, this information can be used to estimate the time of an event. That is, again consider a signal with phase

$$\Theta = \omega t - kx \quad (14)$$

where now  $t$  is unknown, but  $\Theta$  can be measured at known frequencies  $\omega$ . A single measurement of  $\Theta$  at some single frequency  $\omega = \omega_0$  is useless for estimating  $t$ , but since we observe that

$$t = \frac{d\Theta}{d\omega} \quad (15)$$

we can estimate  $t$  from observing how  $\Theta$  changes over a band of frequencies. The precision of our estimate (i.e. time resolution) depends on how wide in frequency (i.e. bandwidth) we observe the phase  $\Theta$ .

Now consider once again a signal with phase

$$\Theta = \omega t - kx \quad (16)$$

where now  $k$  is unknown, and  $\omega$  and  $t$  are fixed but also unknown, but  $\Theta$  can be measured at known positions  $x$ . We identify the wavenumber

$$k = \frac{d\Theta}{dx} \quad (17)$$

Similarly, the way to estimate position  $x$  is to take  $\Theta$  readings at multiple wavenumbers  $k$  and observe that we can calculate position  $x$  as

$$x = \frac{d\Theta}{dk} \quad (18)$$

This is exactly what SAR imaging is all about.

In two spatial dimensions, the phase is given by

$$\Theta = \omega t - (k_x x + k_y y) \quad (19)$$

If we fix time such that  $\omega t = \phi$ , then this becomes

$$\Theta = \phi - (k_x x + k_y y) = \phi - k_x x - k_y y \quad (20)$$

Consequently, in order to find a unique position  $(x,y)$  we need to vary both wavenumbers  $k_x$  and  $k_y$ , but in an independent manner, so we can tell which is a result of wiggling  $k_x$ , and which is a result of wiggling  $k_y$ . But since we observe that from Figure 1

$$\begin{aligned} k_x &= k \cos \theta, \text{ and} \\ k_y &= k \sin \theta, \end{aligned} \tag{21}$$

we can rewrite the phase at a fixed time as

$$\Theta = \phi - k \cos(\theta)x - k \sin(\theta)y. \tag{22}$$

and note that we can equivalently independently wiggle  $k$  and  $\theta$ . This is exactly what a SAR does, where the pulse bandwidth is related to wiggling  $k$ , and the synthetic aperture is related to wiggling  $\theta$ .

Note that in three spatial dimensions we have

$$\Theta = \phi - k_x x - k_y y - k_z z \tag{23}$$

and recognize that to extract the  $z$  position we need to independently wiggle  $k_z$ . This is exactly what the second antenna phase center (offset in elevation) is all about in Interferometric SAR (IFSAR).

### Fourier Space of a Scene

Consider a 2-dimensional scene out there with brightness (perhaps complex) function that varies with spatial position, say

$$\sigma(x, y) = \text{2-D space-varying function.} \tag{24}$$

If we take the 2-D Fourier Transform of this with respect to the spatial coordinates  $x$ , and  $y$ , we end up with a new function

$$S(k_x, k_y) = \int_{-\infty}^{\infty} \int_{-\infty}^{\infty} \sigma(x, y) e^{-j(k_x x + k_y y)} dx dy \tag{25}$$

that describes how much brightness (energy) we have for specific combinations of wavenumbers  $k_x$  and  $k_y$ . That is, any particular location  $(x_0, y_0)$  will induce specific wiggles across wavenumbers  $k_x$  and  $k_y$  with the same energy as exists at that location. Equivalently, a specific set of wiggles in  $k_x$  and  $k_y$  at some energy level will set the brightness at a specific location  $(x_0, y_0)$ .

Consequently, if we can gather enough information in the ‘wavenumber’ domain, which we now also call the ‘Fourier space’ of the scene, we should be able to estimate what the

scene content  $\sigma(x, y)$  is. We don't really need to know the entire Fourier space of the scene, but as it turns out, the size of the region that we do know ultimately sets the precision (resolution) with which we can estimate scene content. As we shall see, this is exactly what a SAR does.

This also extends to 3-D scenes very nicely.

The notion that only a relatively small region of the Fourier space of the scene is needed to form an image is well known.<sup>5</sup> However, less appreciated is the fact that even optical imagery that has been appropriately 'bandpass' filtered yields images that are very SAR-like.<sup>6</sup>

### 3 SAR Imaging in a 2-D World

Polar Format processing was first developed for Inverse-SAR (ISAR) operation, where the radar position was fixed and the target was placed on a rotating turn-table.<sup>1</sup> We, however, will develop it from the viewpoint of a stationary scene, with moving radar.

Consider a 2-D world where the z-dimension doesn't exist. Furthermore, consider the radar geometry of Figure 2. In this geometry we define

$$\begin{aligned}
 \mathbf{s} &= \text{the spatial location of a point target, with coordinates } (s_x, s_y), \\
 \mathbf{r}_c &= \text{the location of the radar, with coordinates } (r_x, r_y), \text{ and} \\
 \mathbf{r}_s &= \mathbf{r}_c - \mathbf{s} = \text{relation of radar location to the point target location.}
 \end{aligned} \tag{26}$$

We will presume for convenience a linear frequency modulated (LFM) transmitted pulse given by

$$X_T(t) = A_T \text{rect}\left(\frac{t}{T}\right) \cos\left(\omega t + \frac{\gamma}{2} t^2\right) \tag{27}$$

where

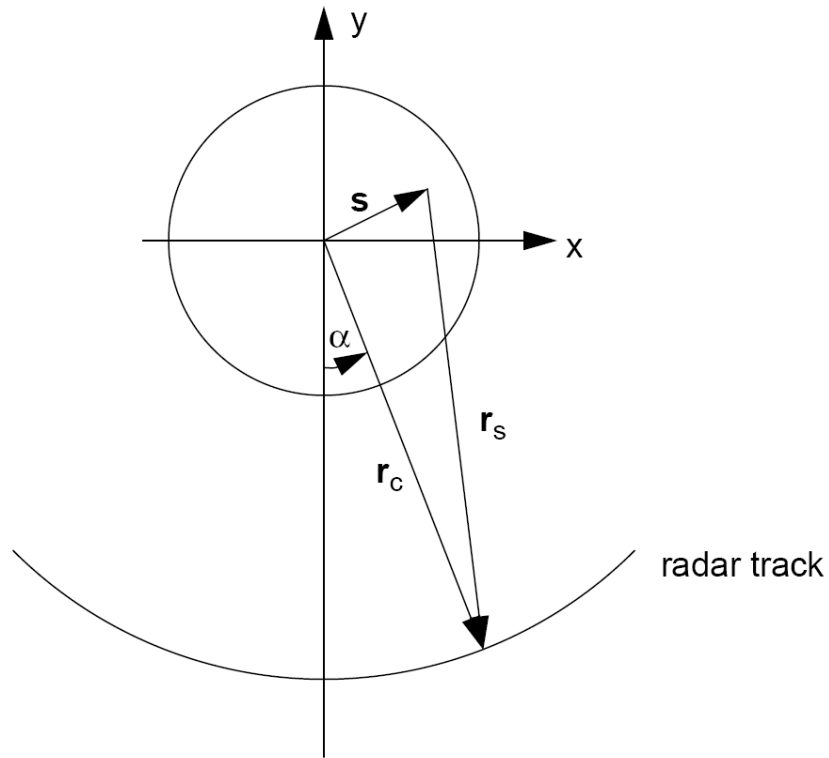


Figure 2. Data collection geometry in a 2-D world.

$$\begin{aligned}
\omega &= \text{center frequency of the transmitted pulse,} \\
\gamma &= \text{chirp rate of the transmitted pulse,} \\
A_T &= \text{amplitude of the transmitted pulse, and} \\
T &= \text{duration of transmitted pulse.}
\end{aligned} \tag{28}$$

We note that the instantaneous frequency of the transmitted signal is

$$\omega_{\text{inst}} = \omega + \gamma t \tag{29}$$

and that the signal bandwidth (for large time-bandwidth product signals used by most SAR systems) is  $\gamma T$  rad/s, or  $\gamma T/(2\pi)$  Hz.

The received echo will be a scaled and time delayed version of the transmitted signal, namely

$$X_R(t) = \frac{A_R}{A_T} \sigma(\mathbf{s}) X_T(t - t_s) = A_R \sigma(\mathbf{s}) \text{rect}\left(\frac{t - t_s}{T}\right) \cos\left(\omega(t - t_s) + \frac{\gamma}{2}(t - t_s)^2\right), \tag{30}$$

where

$$\begin{aligned}
A_R &\text{ is the nominal amplitude of the received echo, and} \\
\sigma(\mathbf{s}) &\text{ is the reflectivity of the target at } \mathbf{s}.
\end{aligned} \tag{31}$$

The echo delay time with respect to the target depends on the distance to the target and the speed of wave propagation, and is

$$t_s = \frac{2}{c} |\mathbf{r}_s|. \tag{32}$$

In reality, a scene will typically be composed of more than just a point target, which means that the received signal is really an integral over all  $\mathbf{s}$  of all the responses from any  $\mathbf{s}$ . That is, this is a linear system for which superposition holds. Nevertheless, to keep the ideas simple, we will continue with the presumption of a single point target.

The echo delay time with respect to the scene center is given by

$$t_c = \frac{2}{c} |\mathbf{r}_c|. \tag{33}$$

For the collection geometry proposed in Figure 1, wherein the radar perfectly orbits the scene center at constant range, this echo delay time is also a constant.

De-chirping this (stretch processing) and using quadrature demodulation yields a video signal of the approximate form

$$X_V(t) \approx A_R \sigma(\mathbf{s}) \text{rect}\left(\frac{t-t_c}{T}\right) \exp j\{\omega(t_c - t_s) + \gamma(t-t_c)(t_c - t_s)\}. \quad (34)$$

We are ignoring the residual video phase error term. We can rewrite this as

$$X_V(t') \approx A_R \sigma(\mathbf{s}) \text{rect}\left(\frac{t'}{T}\right) \exp j\{[\omega + \gamma t'](t_c - t_s)\} \quad (35)$$

where  $t' = t - t_c$  just to make things look a little simpler, but it is important to note that  $t'$  does vary over the interval  $-T/2$  to  $T/2$ . Note that the quantity  $[\omega + \gamma t']$  is again an instantaneous frequency expression.

If we completely sample this interval with an Analog to Digital converter at times

$$t' = iT_s \quad (36)$$

where

$$\begin{aligned} i &= \text{sample index such that } -I/2 \leq i \leq I/2 - 1, \text{ and} \\ T_s &= T/I = \text{ADC sample spacing,} \end{aligned} \quad (37)$$

then the sampled video signal becomes

$$X_V(i) \approx A_R \sigma(\mathbf{s}) \exp j\{[\omega + \gamma T_s i](t_c - t_s)\}. \quad (38)$$

Note that each sample index  $i$  represents a different instantaneous frequency  $[\omega + \gamma T_s i]$ . The time difference quantity  $(t_c - t_s)$  can be related to ranges and expanded to

$$(t_c - t_s) \approx \frac{2}{c} (s_x \sin \alpha - s_y \cos \alpha). \quad (39)$$

This expression does ignore some higher-order error terms that account for wavefront curvature, but is sufficient for the task at hand. Nevertheless, this can be inserted into the video signal expression and rearranged to

$$X_V(i) \approx A_R \sigma(\mathbf{s}) \exp j\left\{\frac{2}{c} [\omega + \gamma T_s i] (s_x \sin \alpha - s_y \cos \alpha)\right\}. \quad (40)$$

Recall that if we divide a frequency by the velocity of propagation, we get a wavenumber quantity. Consequently, let us set

$$\frac{2}{c} [\omega + \gamma T_s i] = k(i) = \text{wavenumber whose value depends on index } i. \quad (41)$$

Note that the wavenumber is ‘wiggled’ across the index  $i$ . The scale factor 2 results from the round trip that is required by the pulse. One might view this as effectively cutting the propagation velocity in half. In any case, we can rewrite the video signal as

$$X_V(i) \approx A_R \sigma(\mathbf{s}) \exp j \{ (k(i) \sin \alpha) s_x - (k(i) \cos \alpha) s_y \}. \quad (42)$$

Note the similarity of the phase to equation (22).

A SAR will vary index  $i$  within any single pulse, and will vary  $\alpha$  from pulse to pulse. The wavenumber variation in index  $i$  is defined by the bandwidth of the chirp. The variation in  $\alpha$  defines the synthetic aperture. Discrete pulses from the radar define samples in  $\alpha$ . Let us for the moment presume constant increments in the samples of  $\alpha$  such that

$$\alpha = d\alpha n \quad (43)$$

where

$$\begin{aligned} d\alpha &= \text{the angular increment in } \alpha \text{ between pulses, and} \\ n &= \text{an index of pulse number such that } -N/2 \leq n \leq N/2 - 1. \end{aligned} \quad (44)$$

The video signal then becomes

$$X_V(i, n) \approx A_R \sigma(\mathbf{s}) \exp j \{ (k(i) \sin(d\alpha n)) s_x - (k(i) \cos(d\alpha n)) s_y \}. \quad (45)$$

We can define wavenumber components now as functions of indices, as

$$\begin{aligned} k_x(i, n) &= k(i) \sin(d\alpha n), \text{ and} \\ k_y(i, n) &= -k(i) \cos(d\alpha n), \end{aligned} \quad (46)$$

and rewrite the video signal as

$$X_V(i, n) \approx A_R \sigma(\mathbf{s}) \exp j \{ k_x(i, n) s_x + k_y(i, n) s_y \}. \quad (47)$$

Clearly, to uniquely resolve spatial location  $(s_x, s_y)$ , we need to identify independent wiggles of  $k_x(i, n)$  and  $k_y(i, n)$ , which can be done with independent wiggles of indices  $i$  and  $n$ .

Each individual sample of a SAR data set (phase history) corresponds to a specific pulse index  $n$ , and a specific video time index  $i$ , and hence corresponds to a unique 2-D wavenumber. Consequently, each individual phase history sample is a unique point in the Fourier space of the scene.

We now ask “So what does the data region look like in Fourier space?” More specifically, “At what wavenumber combinations does the collected phase history fall?”

We want to find at what  $(k_x, k_y)$  location in Fourier space do the phase history samples fall, if the phase history samples are identified at specific index combinations  $i$  and  $n$ . With malice of forethought we identify the displacement from the wavenumber origin as

$$\sqrt{k_x^2(i, n) + k_y^2(i, n)} = k(i) = \frac{2}{c} [\omega + \gamma T_s i]. \quad (48)$$

That is,  $k(i)$  is the distance of the  $i^{\text{th}}$  sample from the Fourier-space origin. Similarly we define the wavenumber location angular displacement from the  $k_y$  axis as

$$\text{atan}\left(\frac{k_x(i, n)}{k_y(i, n)}\right) = \pi - d\alpha n. \quad (49)$$

That is,  $d\alpha n$  is the angular offset of the  $n^{\text{th}}$  sample from the negative  $k_y$  axis in Fourier space.

Clearly, the indices  $i$  and  $n$  are indices to samples on a polar grid in Fourier space. That is, the phase history sample array corresponds to Fourier space samples on polar grid locations. This polar raster of positions is illustrated in Figure 3. This entire set of sample locations define an ‘aperture’ or ‘window’ into the Fourier space of the scene. The required density of the sample spacing depends (via Nyquist criteria) on the ‘space-width’ or spatial extent of the scene. This typically depends on the antenna beamwidth and the radar video (or perhaps IF) bandwidth.

In any case, all we have to do is transform this ‘wavenumber’ domain data into the ‘space’ domain and we have an image of the scene. This is easier said than done.

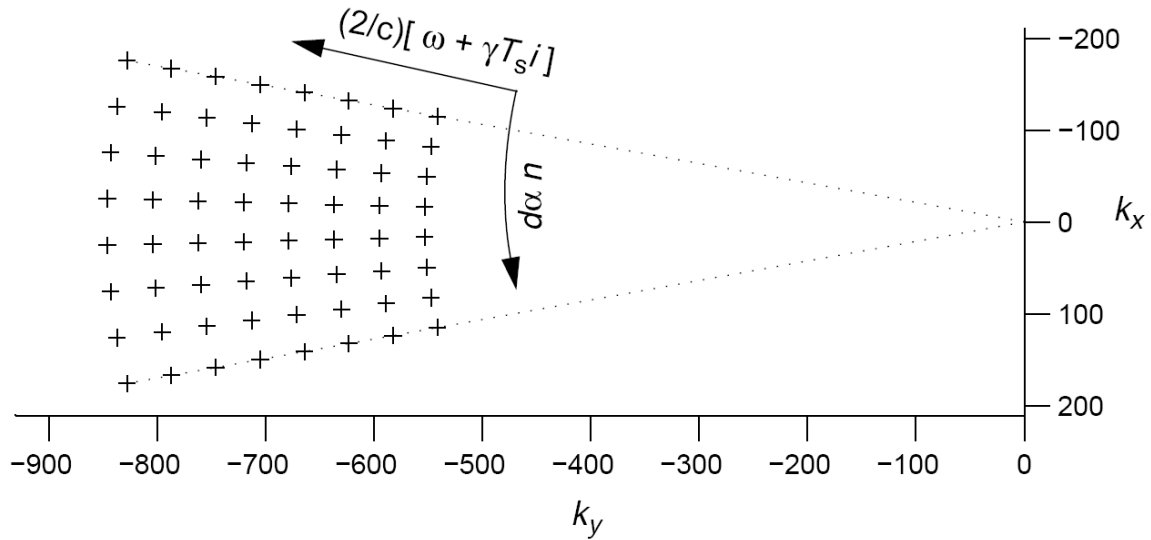


Figure 3. Polar grid of phase history data locations in the Fourier space of the scene in a 2-D world.

### 3.1 General Image Transform

Recall the video signal expression

$$X_V(i, n) \approx A_R \sigma(\mathbf{s}) \exp j \{ k_x(i, n) s_x + k_y(i, n) s_y \}. \quad (50)$$

The question now is “How do we extract the space-domain image from the Fourier-domain phase history data?” The answer, of course, is some sort of 2-Dimensional Fourier Transform.

If the Fourier-space data were continuous, the transform to yield a spatial image would be

$$S(x, y) = \int_{-\infty}^{\infty} \int_{-\infty}^{\infty} X_V e^{-j(k_x x + k_y y)} dk_x dk_y. \quad (51)$$

For the discrete sampled phase history data, the 2-D Discrete Fourier Transform (DFT) yields

$$S(x, y) = \sum_i \sum_n X_V(i, n) e^{-j(k_x(i, n)x + k_y(i, n)y)}. \quad (52)$$

This is true for any  $(x, y)$  position in the SAR image. Typically we quantize the  $(x, y)$  positions to specific multiples of some pixel spacing, say where we are interested in

$$(x, y) = (\delta_x u, \delta_y v) \quad (53)$$

where  $\delta_x$  and  $\delta_y$  are pixel spacings in  $x$  and  $y$  directions respectively, and  $u$  and  $v$  are pixel indices in  $x$  and  $y$  directions respectively. Consequently

$$S(\delta_x u, \delta_y v) = \sum_i \sum_n X_V(i, n) e^{-j(k_x(i, n)\delta_x u + k_y(i, n)\delta_y v)}. \quad (54)$$

This formula would work just great, insofar as forming an image is concerned. It is limited only to the extent that equation (50) is a suitable model for the phase history data. It implements a 2-D matched filter to data described by equation (50). The problem is, a direct implementation of this equation means selecting a particular  $(u, v)$  coordinate, and performing a 2-D sum over all phase history samples at all combinations of indices  $i$  and  $n$ . This would then be repeated for every combination of image coordinates  $u$  and  $v$  that was of interest. This is a brute-force technique, and computationally expensive. Unfortunately, the non-linear nature of the Fourier kernel  $k_x(i, n)\delta_x u + k_y(i, n)\delta_y v$  is not well suited to efficient calculation by “Fast” transforms, such as the 2-D Fast Fourier Transform (FFT). This is because of the polar grid nature of the phase history sample placement in Fourier space.

What would be well suited is a kernel of the form  $C_x nu + C_y iv$  where  $C_x$  and  $C_y$  are constants. That is, what would really be nice is if the transform to the image domain looked more like

$$S(\delta_x u, \delta_y v) = \sum_i \sum_n X_V(i, n) e^{-j(C_x nu + C_y iv)}. \quad (55)$$

Fourier-space locations that would meet this format constitute a Cartesian grid of sample locations as illustrated in Figure 4, rather than the polar grid of Figure 3. With samples on a Cartesian grid, a 2-D DFT would work just great, and be much less computationally expensive. Oh, well....

Note: The 2-D DFT may be rewritten with scaled image indices to perhaps a more familiar form more suitable for the 2-D FFT

$$S\left(\left(\frac{\delta_x C_x N}{2\pi}\right)u', \left(\frac{\delta_y C_y I}{2\pi}\right)v'\right) = \sum_i \sum_n X_V(i, n) e^{-j\left(\frac{2\pi}{N}nu' + \frac{2\pi}{I}iv'\right)}. \quad (56)$$

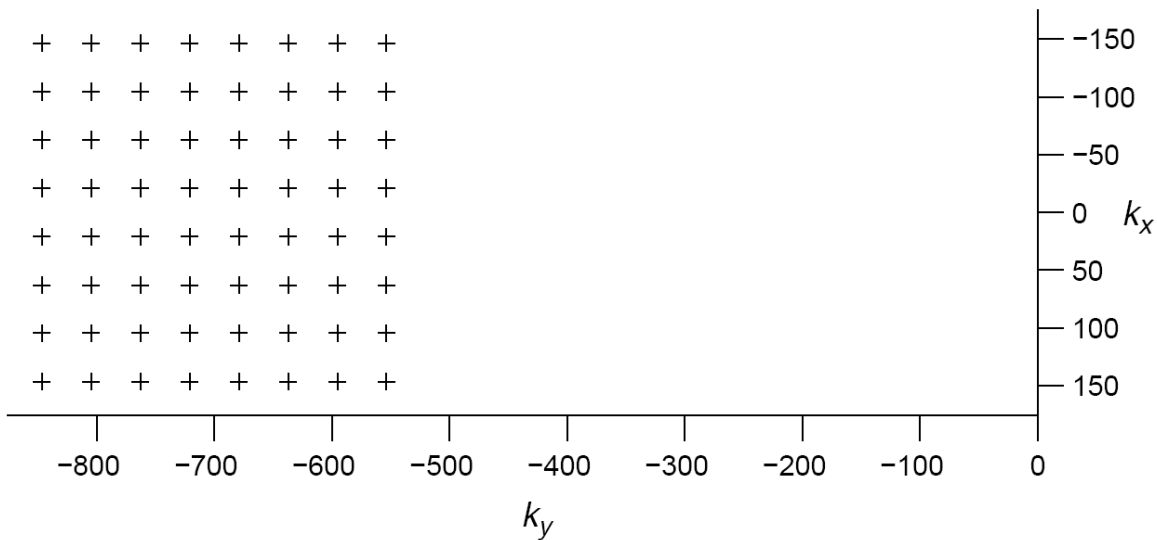


**Figure 4. Desired Cartesian grid locations in Fourier space for easy processing of phase history data.**

### 3.2 Small Aperture Approximations

If the ‘aperture’ in Fourier space is relatively small then some useful simplifying approximations can be made. Note that these conditions are tantamount to limiting the SAR images to coarser resolutions, in both dimensions.

If the signal bandwidth is small, that is,

$$\gamma T \ll \omega, \quad (57)$$

and the spread of polar angles is small,

$$d\alpha N \ll 1, \quad (58)$$

then we can approximate

$$\begin{aligned} k_x(i, n) &\approx k(0)d\alpha n = \frac{2}{c}\omega d\alpha n, \text{ and} \\ k_y(i, n) &\approx -k(i)\cos(0) = -\frac{2}{c}\omega - \frac{2}{c}\gamma T_s i. \end{aligned} \quad (59)$$

This allows the phase history data to be modeled by

$$X_V(i, n) \approx A_R \sigma(\mathbf{s}) \exp j \left\{ \left( \frac{2}{c} \omega d\alpha n \right) s_x + \left( -\frac{2}{c} \omega - \frac{2}{c} \gamma T_s i \right) s_y \right\}. \quad (60)$$

This, in turn, allows the transform to the image domain to be approximated by

$$S(\delta_x u, \delta_y v) \approx \sum_i \sum_n X_V(i, n) e^{-j \left\{ \left( \frac{2}{c} \omega d\alpha \delta_x \right) nu + \left( -\frac{2}{c} \gamma T_s \delta_y \right) iv \right\}}. \quad (61)$$

Note that this is of the form in equation (55). The assumption is that for small polar angles, and small signal bandwidths, a polar grid is very nearly equivalent to a Cartesian grid. Consequently, the image can be formed as if the Fourier space phase history samples were already on a Cartesian grid. This conveniently requires only the conventional 2-D DFT (or FFT) to make the transformation from Fourier space to image domain.

This is often referred to as merely “2-D DFT processing” or “linear range-Doppler processing”. It seems to work fairly well for modest scene sizes at Ku-band down to perhaps 1-m resolutions. However, as resolutions begin to approach the wavelength of the radar, these approximations fail horribly. The polar grid nature of the phase history data can no longer be ignored.

### 3.3 Polar Reformatting

Because of the finite scene extent that makes it through the antenna, presummer, IF and video filters, we say the data is space-limited (sort of like band-limited, but in the other domain). Consequently, strong correlation exists over small neighborhoods in the Fourier domain (phase history data). In fact we have presumed just this in selecting ADC sampling rates and radar PRFs to allow sampled phase history data to accurately represent the nature of the Fourier space of the scene. So what????

This means that we should be able to guess (calculate) pretty well what the Fourier space values should look like between the phase history samples that we actually have. That is, we should be able to interpolate between the Fourier space samples we have pretty well. But why???

The data that we have is on a polar grid, but what we want is data on a Cartesian grid. What comes to mind is to ‘resample’ the data from the polar grid it is on, to the Cartesian grid that is more suitable for easy transformation to the image domain. This involves interpolating the phase history data to other more suitable sample points in the Fourier domain of the scene. How???

While this can be done as a 2-D interpolation operation, it is more typically done as two separate 1-D interpolation operations.

What we have is data described by

$$X_V(i, n) \approx A_R \sigma(\mathbf{s}) \exp j \{ k_x(i, n) s_x + k_y(i, n) s_y \}, \quad (62)$$

where the Fourier domain samples are located at

$$\begin{aligned} k_x(i, n) &= \frac{2}{c} [\omega + \gamma T_s i] \sin(d\alpha n), \text{ and} \\ k_y(i, n) &= -\frac{2}{c} [\omega + \gamma T_s i] \cos(d\alpha n). \end{aligned} \quad (63)$$

What we want is interpolation to new Fourier domain sample positions such that

$$X_V(i', n') \approx A_R \sigma(\mathbf{s}) \exp j \{ k_x(n') s_x + k_y(i') s_y \}, \quad (64)$$

where the new Fourier domain samples are at locations where the wavenumber components use decoupled indices

$$\begin{aligned} k_x(n') &= \frac{2}{c} \omega d\alpha n', \text{ and} \\ k_y(i') &= -\frac{2}{c} [\omega + \gamma T_s i']. \end{aligned} \quad (65)$$

The two step process is typically implemented as follows

1. First we interpolate in a radial direction such that

$$k_y(i, n) = k_y(i'), \quad (66)$$

that is, such that

$$[\omega + \gamma T_s i] \cos(d\alpha n) = [\omega + \gamma T_s i']. \quad (67)$$

This is accomplished by picking an integer index value for  $i'$ , and finding the corresponding non-integer value for  $i$  for which new data must be interpolated, and doing so for each sample index  $i'$ , and each pulse index  $n$ . For example,

$$i = \frac{[\omega + \gamma T_s i'] - \omega}{\gamma T_s \cos(d\alpha n)} = \frac{1}{\cos(d\alpha n)} \left[ \frac{\omega}{\gamma T_s} + i' \right] - \frac{\omega}{\gamma T_s}. \quad (68)$$

Data so interpolated makes  $k_y$  independent of azimuth index  $n$ . However, in doing so, we have also altered somewhat the nature of  $k_x$  since it also depended on index  $i$  (it now depends on index  $i'$ ). Now we have

$$k_x(i', n) = \frac{2}{c} \left[ \frac{\omega + \gamma T_s i'}{\cos(d\alpha n)} \right] \sin(d\alpha n) = \frac{2}{c} [\omega + \gamma T_s i'] \tan(d\alpha n). \quad (69)$$

These new partially reformatted wavenumber locations constitute a trapezoidal shape and are illustrated in Figure 5. Note how values for  $k_y$  are ‘lined-up’, but values for  $k_x$  still exhibit an angular increment.

2. Second, we interpolate in the azimuth direction such that

$$k_x(i', n) = k_x(n'), \quad (70)$$

that is, such that

$$[\omega + \gamma T_s i'] \tan(d\alpha n) = \omega d\alpha n'. \quad (71)$$

This is accomplished by picking an integer value for  $n'$ , and finding the corresponding non-integer value for  $n$  for which new data must be interpolated, and doing so for each new ADC sample index  $i'$ , and for each  $n'$ . For example

$$n = \frac{\text{atan}\left(\frac{\omega d \alpha n'}{\omega + \gamma T_s i'}\right)}{d \alpha}. \quad (72)$$

Data so interpolated makes  $k_x$  independent of ADC sample index  $i$  and/or  $i'$ .

The final result is Fourier space data described by equation (64) and illustrated in Figure 4. That is, the newly interpolated phase history data is laid out on a Cartesian grid in the Fourier space of the scene.

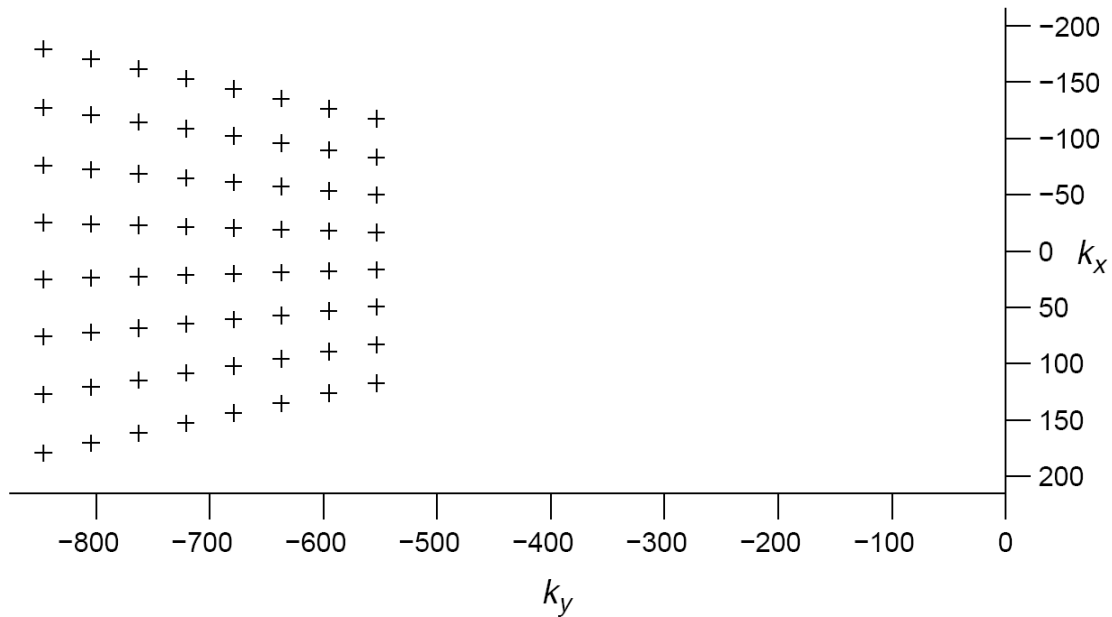


**Figure 5.** Trapezoidal grid of phase history data locations in Fourier space after first stage of polar reformatting (data interpolation).

### 3.4 Polar Reformatting with Real-time Motion Compensation

We note that in the previous section, the 2-D interpolation operation to a Cartesian grid was carried out in two stages, each using 1-D interpolations. The first step adjusted the radial position of the wavenumber samples, and the second step adjusted the  $k_x$  position of the wavenumber samples.

We also recall that the radial wavenumber distance is  $k(i) = (2/c)[\omega + \gamma T_s i]$ , and the interpolation operation is an adjustment to non-integer values of index  $i$ , for the purpose of pulse-to-pulse adjustments in  $k(i)$ . However, from this expression we also note that a pulse-to-pulse adjustment to  $k(i)$  might also be accomplished by pulse-to-pulse adjustments to any of  $\omega$ ,  $\gamma$ , and/or  $T_s$ . Let a subscript  $n$  denote adjustability on a pulse-to-pulse basis. Then what we really desire from the first stage of interpolation is that

$$[\omega_n + \gamma_n T_{s,n} i] \cos(\alpha_n) = [\omega_0 + \gamma_0 T_{s,0} i'] \quad (73)$$

where the zero subscript denotes a nominal constant value.

This equivalence allows us to keep  $i = i'$  if we adjust on a pulse-to-pulse basis

$$\omega_n = \frac{\omega_0}{\cos(\alpha_n)}, \text{ and } \gamma_n T_{s,n} = \frac{\gamma_0 T_{s,0}}{\cos(\alpha_n)}. \quad (74)$$

Consequently, adjusting on a pulse-to-pulse basis the radar frequency  $\omega_n$  and chirp rate  $\gamma_n$  (or equivalently ADC sample spacing  $T_{s,n}$ ) we can collect data that already has the first half of the polar reformatting implemented. That is, these real-time waveform and/or sampling adjustments allow collecting data directly on the trapezoidal grid of Figure 5.

The expression for the phase history data so collected becomes

$$X_V(i, n) \approx A_R \sigma(\mathbf{s}) \exp j \{ k_x(i, n) s_x + k_y(i) s_y \}, \quad (75)$$

where the Fourier domain samples are located at

$$\begin{aligned} k_x(i, n) &= \frac{2}{c} [\omega_0 + \gamma_0 T_{s,0} i] \tan(\alpha_n), \text{ and} \\ k_y(i) &= -\frac{2}{c} [\omega_0 + \gamma_0 T_{s,0} i]. \end{aligned} \quad (76)$$

Clearly, we have removed the dependence of  $k_y$  on index  $n$ , merely by how we collect the phase history data. This is a good thing. While it would be desirable to remove the

dependence of  $k_x$  on index  $i$  in some similar real-time manner, unfortunately we haven't quite figured out how to do this yet. This would require somehow adjusting parameters such that

$$[\omega_0 + \gamma_0 T_{s,0} i] \tan(\alpha_n) = \omega_0 d \alpha_n. \quad (77)$$

For reasons that will become apparent shortly, it is desirable to get 'part-way' there by choosing pulse angles  $\alpha_n$  such that

$$\tan(\alpha_n) = d \alpha_n. \quad (78)$$

This allows us to collect data at wavenumber locations

$$k_x(i, n) = \frac{2}{c} [\omega_0 + \gamma_0 T_{s,0} i] d \alpha_n, \quad (79)$$

which says that for any ADC index value for  $i$ , that sample spacing is constant across  $n$ . This still describes a trapezoidal aperture in Fourier space, and is illustrated in Figure 6, but with the subtle difference that locations for  $k_x$  now exhibit a linear increment instead of an angular increment.

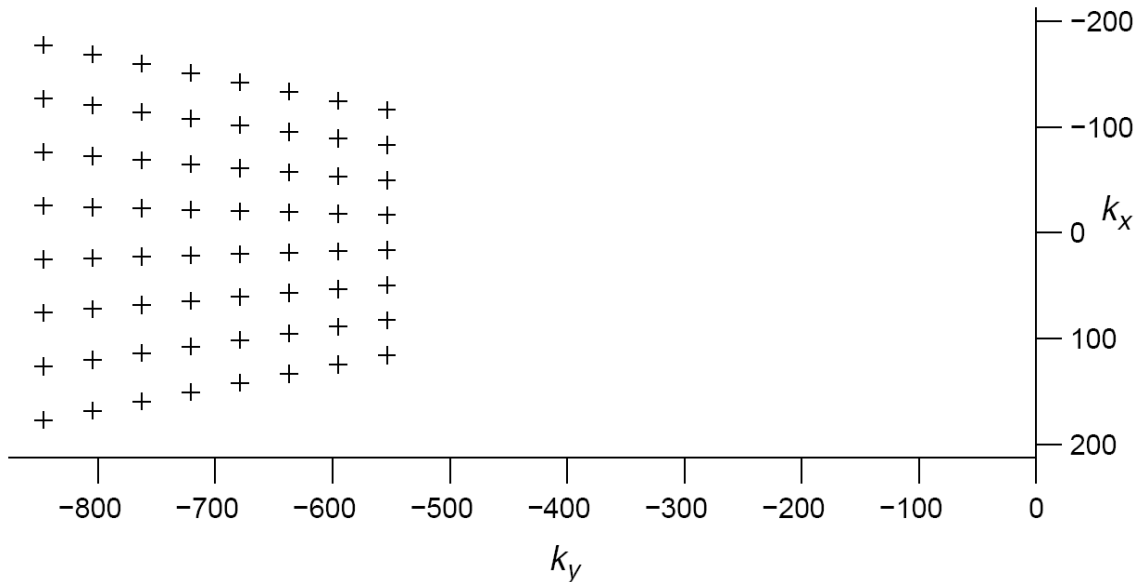


**Figure 6. Trapezoidal locations of phase history data in Fourier space resulting from real-time adjustments in radar frequency, chirp rate, and pulse timing.**

That is, the expression for the phase history data so collected becomes

$$X_V(i, n) \approx A_R \sigma(\mathbf{s}) \exp j \{ k_x(i, n) s_x + k_y(i) s_y \}, \quad (80)$$

where the Fourier domain samples are located at

$$\begin{aligned} k_x(i, n) &= \frac{2}{c} [\omega_0 + \gamma_0 T_{s,0} i] d\alpha n, \text{ and} \\ k_y(i) &= -\frac{2}{c} [\omega_0 + \gamma_0 T_{s,0} i]. \end{aligned} \quad (81)$$

This is now the nature of the raw phase history data. Completing the polar reformatting is now simplified to merely a linear resampling across index  $n$  in the following manner.

We interpolate in the azimuth direction such that

$$[\omega_0 + \gamma_0 T_{s,0} i] d\alpha n = \omega_0 d\alpha n'. \quad (82)$$

This is accomplished by picking an integer value for  $n'$ , and finding the corresponding non-integer value for  $n$  for which new data must be interpolated, and doing so for each new ADC sample index  $i$ . For example

$$n = \frac{\omega_0 n'}{\omega_0 + \gamma_0 T_{s,0} i} = \left( \frac{1}{1 + \frac{\gamma_0 T_{s,0} i}{\omega_0}} \right) n'. \quad (83)$$

Data so interpolated makes  $k_x$  independent of ADC sample index  $i$ .

That is, once again we have

$$X_V(i, n) \approx A_R \sigma(\mathbf{s}) \exp j \{ k_x(n') s_x + k_y(i) s_y \}. \quad (84)$$

where the Fourier domain samples are located at

$$\begin{aligned} k_x(n') &= \frac{2}{c} [\omega_0] d\alpha n', \text{ and} \\ k_y(i) &= -\frac{2}{c} [\omega_0 + \gamma_0 T_{s,0} i]. \end{aligned} \quad (85)$$

This is good.

### 3.5 Polar Reformatting using a Chirped Z-Transform

Fourier-domain data collected on the grid of Figure 6 (trapezoidal aperture with linear spacing in  $k_x$ ) allows some additional processing advantages.

In the prior section we suggested that the data be resampled prior to a 2-D DFT. We note that a 2-D DFT is normally composed of successive 1-D DFTs, perhaps first in index  $i$ , and then in index  $n$ , or vice versa.

Clearly, beginning with data of Figure 6, one set of operations that would achieve an ‘image’ is the following

1. linear resampling in azimuth (index  $n$ ),
2. azimuth DFT (or FFT) across index  $n$ , and
3. range DFT across index  $i$ .

We observe now that the first two of these operations can be combined into a single operation, namely the Chirped Z-Transform (CZT).

This would allow the sequence of events to become

1. azimuth CZT across index  $n$ , and
2. range DFT across index  $i$ .

The result of using this CZT approach on data collected as in Figure 6 is an image equivalent to the more traditional 2-D DFT of polar reformatted data of the more naive data set illustrated in Figure 3. Furthermore, this CZT approach requires no overt interpolation steps (although it does require the somewhat more complex CZT itself).

Now for the details.

#### DFT Background

Consider a generic function  $y(t)$  that is sampled at a rate  $f_n$  samples per second to yield the indexed samples  $y(n/f_n)$ . A DFT across index  $n$  evaluates the spectrum of this at frequencies  $f$ , by performing

$$Y(f) = \sum_n y\left(\frac{n}{f_n}\right) e^{-j2\pi \frac{f}{f_n} n} . \quad (86)$$

where  $f$  is frequency in Hz.

Basically, plug in whatever  $f$  you are interested in, and out pops the answer.

### FFT Background

To expedite the processing in an efficient manner, the ‘Fast’ version of the DFT was developed and is commonly known as the Fast Fourier Transform (FFT). Its architecture relies on determining specific  $f$ , that is, it requires that

$$f = \frac{f_n}{N} u \quad (87)$$

for some integer index  $u$ . As such, it calculates

$$Y\left(\frac{f_n}{N} u\right) = \sum_n y\left(\frac{n}{f_n}\right) e^{-j\frac{2\pi}{N} un} . \quad (88)$$

Note that the frequency spacing is fixed at  $f_n/N$ .

### CZT Background

Also known as the ‘Chirp Transform Algorithm (CTA)’, the CZT is somewhat more general than the FFT in that it allows finding  $Y(f)$  at arbitrary linearly spaced frequencies.<sup>7</sup> That is, it allows for

$$f = \Delta_f u' \quad (89)$$

for some integer index  $u'$ , where  $\Delta_f$  is an arbitrary constant. Consequently, it calculates

$$Y(\Delta_f u') = \sum_n y\left(\frac{n}{f_n}\right) e^{-j\Delta_f u' n} . \quad (90)$$

One might consider this as a ‘linearly resampled’ version of the FFT output where integer values of  $u'$  correspond to non-integer values of  $u$  as follows

$$u = \frac{N}{f_n} \Delta_f u' . \quad (91)$$

What makes this significant is the frequency scaling property of the Fourier Transform, restated here as

$$\begin{aligned}
\text{If } F\{y(t)\} &= \int_{-\infty}^{\infty} y(t)e^{-j2\pi ft} = Y(f), \\
\text{then } F\{y(at)\} &= \int_{-\infty}^{\infty} y(at)e^{-j2\pi ft} = \frac{1}{|a|} Y\left(\frac{f}{a}\right).
\end{aligned} \tag{92}$$

which also applies to the FFT as

$$\begin{aligned}
\text{If } FFT\left\{y\left(\frac{n}{f_n}\right)\right\}_{|N} &= \sum_n y\left(\frac{n}{f_n}\right) e^{-j\frac{2\pi}{N}un} = Y\left(\frac{f_n}{N}u\right), \\
\text{and } y(n/f_n) \text{ (a length } N \text{ sequence) is resampled to} \\
y(n'/f_n) &= y(an/f_n) \text{ (a length } N' \text{ sequence),} \\
\text{then } FFT\left\{y\left(\frac{n'}{f_n}\right)\right\}_{|N'} &= \sum_n y\left(a\frac{n}{f_n}\right) e^{-j\frac{2\pi}{N'}un} = \frac{N}{N'} Y\left(\frac{f_n}{N} \frac{u}{a}\right),
\end{aligned} \tag{93}$$

This allows that *for a given data set, performing a FFT and then linearly resampling the output, is equivalent to first linearly resampling the data set followed by a FFT.* That is, if linear resampling is involved, it can be done either before or after the FFT, equivalently.

The scale factor  $(N/N')$  depends on any change in sequence length. It does not alter the spectral shape, just the overall gain factor.

The CZT, however, can find this resampled spectrum directly (to within a scale factor) by

$$CZT\left\{y\left(\frac{n}{f_n}\right)\right\}_{\left|\Delta_f = \frac{2\pi}{Na}\right.} = \sum_n y\left(\frac{n}{f_n}\right) e^{-j\Delta_f un} = Y\left(\frac{f_n}{N} \frac{u}{a}\right). \tag{94}$$

This is nice, and particularly useful to SAR image formation.

### 3.6 SAR Image Formation

Let us now return to the model for the motion compensated phase history data, namely

$$X_V(i, n) \approx A_R \sigma(\mathbf{s}) \exp j \{ k_x(i, n) s_x + k_y(i) s_y \}, \quad (95)$$

where the Fourier domain samples are located at

$$\begin{aligned} k_x(i, n) &= \frac{2}{c} [\omega_0 + \gamma_0 T_{s,0} i] d \alpha n, \text{ and} \\ k_y(i) &= -\frac{2}{c} [\omega_0 + \gamma_0 T_{s,0} i]. \end{aligned} \quad (96)$$

We rewrite the data as

$$X_V(i, n) \approx A_R \sigma(\mathbf{s}) \exp j \{ k_y(i) s_y \} \exp j \{ k_x(i, n) s_x \}, \quad (97)$$

and expand it as

$$X_V(i, n) \approx [A_R \sigma(\mathbf{s}) \exp j \{ k_y(i) s_y \}] \exp j \left\{ \frac{2\omega_0}{c} d \alpha s_x \left( 1 + \frac{\gamma_0 T_{s,0}}{\omega_0} i \right) n \right\}. \quad (98)$$

The first transform will be an azimuth transform across index  $n$ . Consequently, the items in the square brackets are constants as far as the transform is concerned.

Let us first visit the results of interpolation with an FFT.

#### Azimuth Processing using Resampling with FFT

Now turning our attention to the exponential with index  $n$  we observe that resampling the data in accordance with equation (83) would yield

$$X_V(i, n') \approx [A_R \sigma(\mathbf{s}) \exp j \{ k_y(i) s_y \}] \exp j \left\{ \frac{2\omega_0}{c} d \alpha s_x n' \right\}. \quad (99)$$

thereby eliminating any dependence on index  $i$  from this phase/frequency term. An FFT across index  $n'$  of this expression would yield

$$\begin{aligned}
FFT_{n'}\{X_V(i, n')\} &\approx [A_R\sigma(\mathbf{s})\exp j\{k_y(i)s_y\}]\sum_{n'} \left( e^{j\left\{\frac{2\omega_0}{c}d\alpha s_x n'\right\}} \right) e^{-j\frac{2\pi}{N'}un'} \\
&\approx [A_R\sigma(\mathbf{s})\exp j\{k_y(i)s_y\}]\sum_{n'} e^{j\left\{\frac{2\omega_0}{c}d\alpha s_x - \frac{2\pi}{N'}u\right\}n'} .
\end{aligned} \tag{100}$$

Performing the summation yields

$$FFT_{n'}\{X_V(i, n')\} \approx [A_R\sigma(\mathbf{s})\exp j\{k_y(i)s_y\}]W_{n'}\left(\frac{2\omega_0}{c}d\alpha s_x - \frac{2\pi}{N'}u\right) \tag{101}$$

where  $W_n()$  represents the image ‘impulse response’ in the azimuth direction, that is, neglecting any window functions

$$W_n(\Omega) = \sum_n e^{j\Omega n} , \tag{102}$$

which has the shape of a sinc() function. This clearly offers a peak response when

$$\frac{2\pi}{N'}u = \frac{2\omega_0}{c}d\alpha s_x , \tag{103}$$

that is independent of index  $i$ .

Now consider substituting a CZT for the interpolation and FFT.

#### Azimuth Processing using CZT

Now consider an application of the CZT directly to equation (98), where

$$\begin{aligned}
CZT_n\{X_V(i, n)\} &\approx [A_R\sigma(\mathbf{s})\exp j\{k_y(i)s_y\}]\sum_n \left( e^{j\left\{\frac{2\omega_0}{c}d\alpha s_x \left(1 + \frac{\gamma_0 T_{s,0}}{\omega_0} i\right) n\right\}} \right) e^{-j\Delta_f un} \\
&\approx [A_R\sigma(\mathbf{s})\exp j\{k_y(i)s_y\}]\sum_n e^{j\left\{\frac{2\omega_0}{c}d\alpha s_x \left(1 + \frac{\gamma_0 T_{s,0}}{\omega_0} i\right) - \Delta_f u\right\}n} .
\end{aligned} \tag{104}$$

If we force  $\Delta_f$  to vary with index  $i$ , that is

$$\Delta_f = \frac{2\pi}{N} \left( 1 + \frac{\gamma_0 T_{s,0}}{\omega_0} i \right). \quad (105)$$

then we have

$$CZT_n \{X_V(i, n)\} \approx [A_R \sigma(\mathbf{s}) \exp j\{k_y(i)s_y\}] \sum_n e^{j \left( 1 + \frac{\gamma_0 T_{s,0}}{\omega_0} i \right) \left\{ \frac{2\omega_0}{c} d\alpha s_x - \frac{2\pi}{N} u \right\} n}. \quad (106)$$

Performing the summation yields

$$CZT_n \{X_V(i, n)\} \approx [A_R \sigma(\mathbf{s}) \exp j\{k_y(i)s_y\}] W_n \left( \left( 1 + \frac{\gamma_0 T_{s,0}}{\omega_0} i \right) \left\{ \frac{2\omega_0}{c} d\alpha s_x - \frac{2\pi}{N} u \right\} \right). \quad (107)$$

This also clearly offers a peak response when

$$\frac{2\pi}{N} u = \frac{2\omega_0}{c} d\alpha s_x, \quad (108)$$

with location that is independent of index  $i$ .

We do note that the image impulse response (IPR) width will vary slightly as a function of index  $i$ , but the peak location will not. This subtle difference between equations (107) and (101) leads to slightly different sidelobe structures.

However, it is also true that the CZT approach uses the entire Fourier space aperture, and not some cropped version of the aperture.

To complete the image formation, we need to transform across index  $i$ .

#### Range Processing with FFT

Consider the results of the azimuth CZT, rearranged here as follows

$$CZT_n \{X_V(i, n)\} \approx \left[ A_R \sigma(\mathbf{s}) W_n \left( \left( 1 + \frac{\gamma_0 T_{s,0}}{\omega_0} i \right) \left\{ \frac{2\omega_0}{c} d\alpha s_x - \frac{2\pi}{N} u \right\} \right) \right] \exp j\{k_y(i)s_y\}. \quad (109)$$

Ignoring the slight fluctuation in the width of the azimuth IPR, and expanding  $k_y(i) = -(2/c)[\omega_0 + \gamma_0 T_{s,0} i]$  yields

$$CZT_n\{X_V(i, n)\} \approx \left[ A_R \sigma(\mathbf{s}) W_n \left( \frac{2\omega_0}{c} d\alpha s_x - \frac{2\pi}{N} u \right) \right] e^{j\left\{-\frac{2}{c}\omega_0 s_y\right\}} e^{j\left\{-\frac{2}{c}\gamma_0 T_{s,0} s_y\right\}} i, \quad (110)$$

which has phase linear in index  $i$ .

Performing a FFT across index  $i$  yields

$$\begin{aligned} FFT_i\{CZT_n\{X_V(i, n)\}\} &= \sum_i CZT_n\{X_V(i, n)\} e^{-j\frac{2\pi}{I}vi} \\ &\approx A_R e^{j\left\{-\frac{2}{c}\omega_0 s_y\right\}} \sigma(\mathbf{s}) W_n \left( \frac{2\omega_0}{c} d\alpha s_x - \frac{2\pi}{N} u \right) \sum_i e^{-j\left\{\frac{2}{c}\gamma_0 T_{s,0} s_y + \frac{2\pi}{I}v\right\}i} \\ &\approx A_R e^{j\left\{-\frac{2}{c}\omega_0 s_y\right\}} \sigma(\mathbf{s}) W_n \left( \frac{2\omega_0}{c} d\alpha s_x - \frac{2\pi}{N} u \right) W_i \left( \frac{2}{c}\gamma_0 T_{s,0} s_y + \frac{2\pi}{I}v \right). \end{aligned} \quad (111)$$

This clearly offers a peak response when

$$\frac{2\pi}{I}v = -\frac{2}{c}\gamma_0 T_{s,0} s_y \quad (112)$$

as well as when

$$\frac{2\pi}{N}u = \frac{2\omega_0}{c} d\alpha s_x. \quad (113)$$

The residual phase perturbation is inconsequential to a magnitude detected image, but could be compensated if so desired.

Equation (111) represents the 2-D complex IPR of a point target.

### 3.7 Complex Data Interpolation

A comprehensive treatment of interpolation and resampling data, especially complex data, is beyond the scope of this report. Good references already exist.<sup>8</sup> We do make the following points, however.

- Here is a science to interpolation. Selecting an interpolation algorithm really should be more than just “let’s use something convenient and see if the images look ok...”
- Complex data interpolation is somewhat harder than it might first appear. A lousy job will add artifacts to the eventual image.
- Interpolation is easier the more the data is oversampled to begin with.
- In classical implementations of polar format processing, the interpolation operations dominate the processing times. Reducing the need for them can dramatically impact the image formation efficiency.

A residual question does remain, however, and that is “Is the CZT approach, in fact, truly more efficient than resampling followed by a FFT?” The answer to this is beyond the scope of this report, but nevertheless very important. A speculative partial answer might be “It will depend on the specific hardware/software tools and architectures available.”

## 4 SAR Imaging in a 3-D World

The prior sections dealt with a 2-dimensional imaging geometry. We now extend this to the 3 spatial dimensions that we all putter around in. Consider the extension of Figure 2 into 3 dimensions with the addition of height, as illustrated in Figure 7.

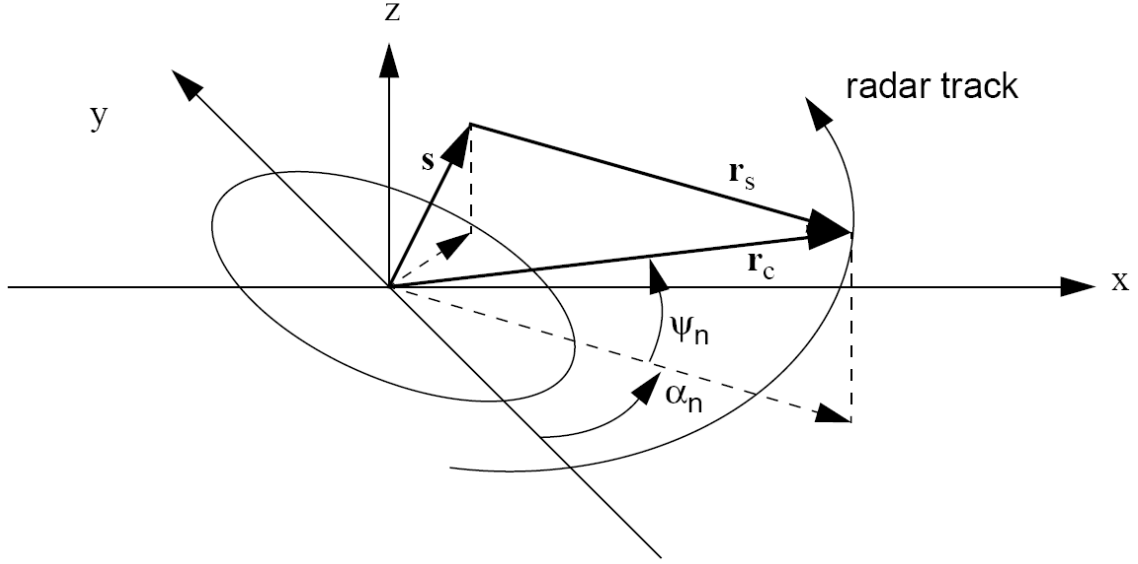


Figure 7. Data collection geometry in a 3-D world.

The target point has coordinates  $(s_x, s_y, s_z)$ , and the radar is elevated at an angle  $\psi_n$ .

In a 3-D world, the radar echo video signal is still given by

$$X_V(i, n) \approx A_R \sigma(\mathbf{s}) \exp j \{ [\omega_n + \gamma_n T_{s,n} i] (t_c - t_s) \}. \quad (114)$$

However, the time difference quantity  $(t_c - t_s)$  is related to range in 3 dimensions, which includes target height and radar height, and must consequently be expanded to

$$(t_c - t_s) \approx \frac{2}{c} (s_x \cos \psi_n \sin \alpha_n - s_y \cos \psi_n \cos \alpha_n + s_z \sin \psi_n). \quad (115)$$

The subscript index  $n$  reflects the quantities that can (including those that we allow to) change from pulse to pulse during a data collection (synthetic aperture). The approximation here is tantamount to presuming planar wavefronts at the target, that is, no wavefront curvature. It is reasonably accurate over small scenes (compared to range).

Note that if  $\sin \psi_n = 0$ , then this degenerates to the 2-D case of the prior section.

## 4.1 Classical Phase History Data Collection

Consider a circular flight path orbiting the scene center. This implies constant range (constant  $t_c$ ), and constant grazing angle ( $\psi_n = \psi_0$ ). Furthermore, consider a constant set of waveform parameters ( $\omega_n = \omega_0$  and  $\gamma_n = \gamma_0$ ), and constant ADC sampling ( $T_{s,n} = T_{s,0}$ ).

The collected phase history data is then described by

$$X_V(i, n) \approx A_R \sigma(\mathbf{s}) \exp j \left\{ k(i) \left( s_x \cos \psi_0 \sin \alpha_n - s_y \cos \psi_0 \cos \alpha_n + s_z \sin \psi_0 \right) \right\}, \quad (116)$$

or expanded into wavenumber components

$$X_V(i, n) \approx A_R \sigma(\mathbf{s}) \exp j \left\{ k_x(i, n) s_x + k_y(i, n) s_y + k_z(i, n) s_z \right\}, \quad (117)$$

where

$$\begin{aligned} k_x(i, n) &= k(i) \cos \psi_0 \sin \alpha_n = \frac{2}{c} [\omega_0 + \gamma_0 T_{s,0} i] \cos \psi_0 \sin \alpha_n, \\ k_y(i, n) &= -k(i) \cos \psi_0 \cos \alpha_n = -\frac{2}{c} [\omega_0 + \gamma_0 T_{s,0} i] \cos \psi_0 \cos \alpha_n, \text{ and} \\ k_z(i, n) &= k(i) \sin \psi_0 = \frac{2}{c} [\omega_0 + \gamma_0 T_{s,0} i] \sin \psi_0. \end{aligned} \quad (118)$$

As with the 2-D case, these wavenumber combinations define coordinates in the Fourier space of the 3-D scene. That is, each individual combination of index  $i$  and index  $n$  defines a unique wavenumber coordinate, that defines a specific point in the Fourier space of the scene. Consequently, a specific phase history data sample (specific sample from a specific pulse) defines the amplitude of a specific location in the Fourier space of the scene. That location is given in spherical coordinates at a distance of  $(2/c)[\omega_0 + \gamma_0 T_{s,0} i]$  from the origin, at an angle from the negative  $k_y$  axis of  $\alpha_n$ , at an elevation of  $\psi_0$  from the  $(k_x, k_y)$  plane. This is illustrated in Figure 8.

Similarly, a collection of phase history data defines a set of samples in the Fourier space of the scene. Data collected in the manner of this section (constant waveform parameters, constant elevation angle) describes a section of a cone, and is illustrated in Figure 9.

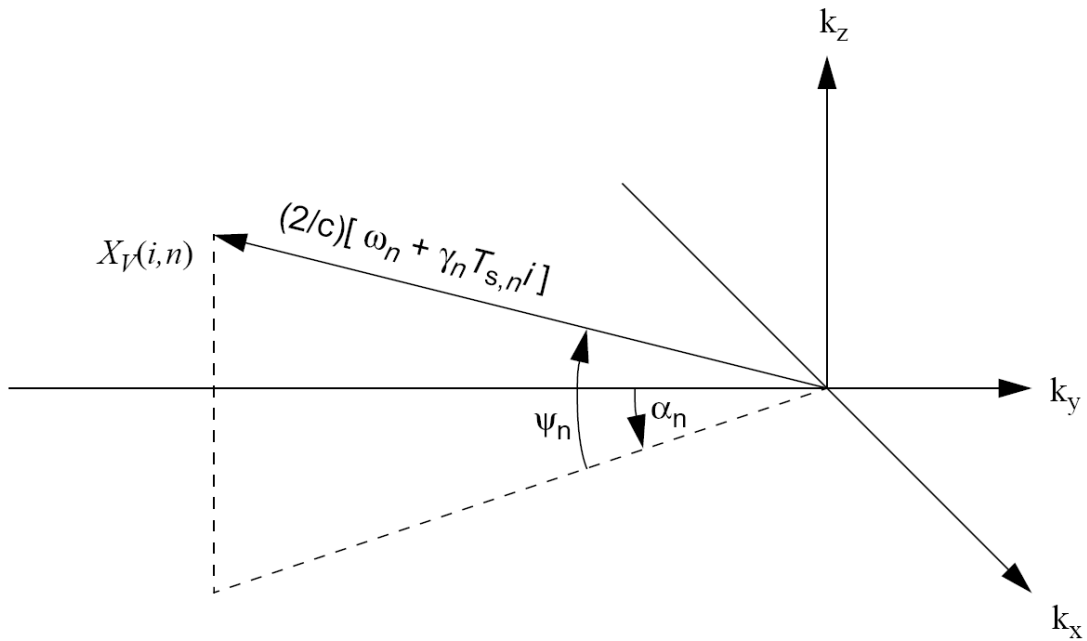


**Figure 8. Location in 3-D Fourier space of a single phase history data sample.**

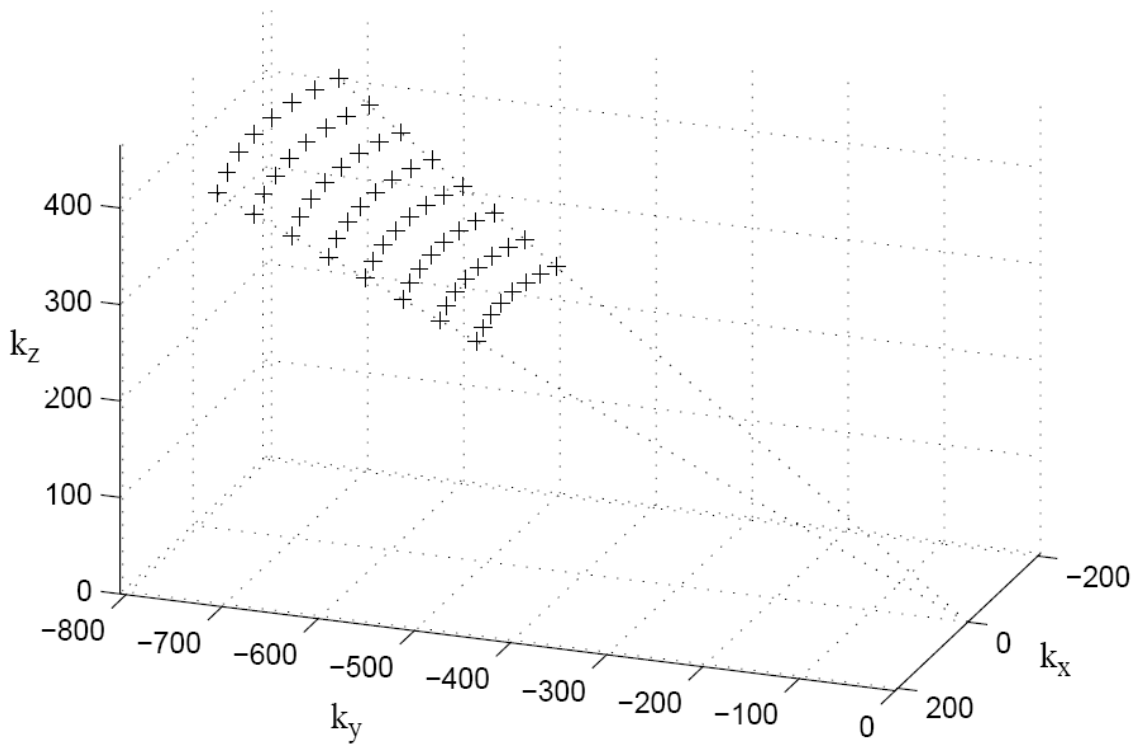


**Figure 9. Location in 3-D Fourier space of a phase history data set, from multiple pulses and multiple ADC samples within any pulse.**

Now for some observations on this phase history data set.

- Our data really is 3 dimensional, that is, it corresponds to 3-D coordinates in the Fourier space of the 3-D scene. As such, seemingly the proper treatment of this data is a 3-D transform to a 3-D image of the scene. And this would be strictly correct.
- However, if we were able to ‘shrink-wrap’ the data locations, we would find that the volume enclosed by the wrap is relatively flat (though not absolutely so). This implies that we have substantially better resolution in the 3-D image in two directions than we have in a third mutually orthogonal direction (this would be the ‘layover’ direction).
- A typical presumption for the scene itself is that it is a flat surface with  $s_z = 0$ . (Remember we are talking SAR here, not IFSAR.) In the 3-D scene this is a presumption of an impulse-like (delta function) response in the  $z$  direction. Consequently, the Fourier space of the data would be characterized by constant values in the  $k_z$  direction. This means that whatever value  $X_V(i, n)$  had at any particular point in Fourier space, the Fourier space value would be unchanged at some other point that had the same  $k_x$  and  $k_y$  values, but a different  $k_z$  value. Consequently, this allows us to project the Fourier space data unchanged to the  $k_z = 0$  plane as in Figure 10, and simply pretend that we collected it there in the first place.
- The projected data is now 2 dimensional, and can be treated as such for transformation to a 2-D image of the 3-D scene. The down side to this is for targets that really do have  $s_z \neq 0$ . The consequence is image layover and height-of-focus problems if  $s_z$  gets too big.

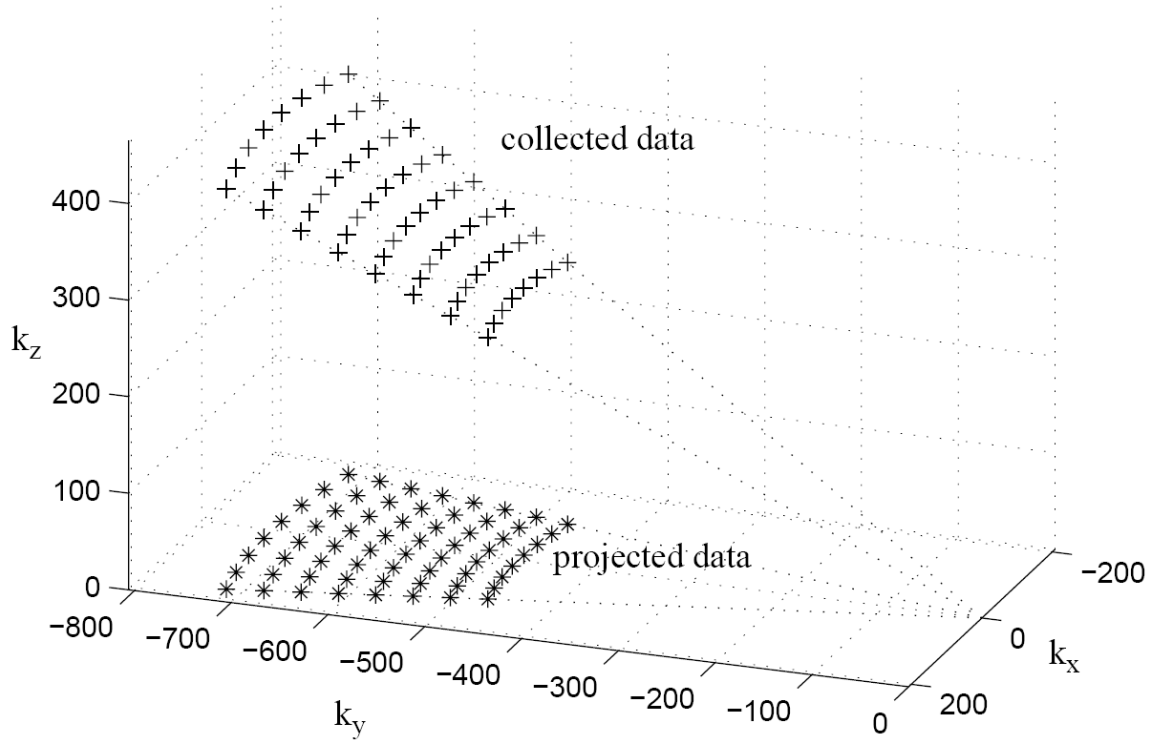


**Figure 10. Fourier space locations of a collected phase history data set, and their projection onto the  $k_z = 0$  plane.**

The presumption that  $s_z = 0$  allows the phase history model to become

$$X_V(i, n) \approx A_R \sigma(\mathbf{s}) \exp j \{ k_x(i, n) s_x + k_y(i, n) s_y \}, \quad (119)$$

where

$$\begin{aligned} k_x(i, n) &= k(i) \cos \psi_0 \sin \alpha_n = \frac{2}{c} [\omega_0 + \gamma_0 T_{s,0} i] \cos \psi_0 \sin \alpha_n, \text{ and} \\ k_y(i, n) &= -k(i) \cos \psi_0 \cos \alpha_n = -\frac{2}{c} [\omega_0 + \gamma_0 T_{s,0} i] \cos \psi_0 \cos \alpha_n. \end{aligned} \quad (120)$$

This describes the projected data. Except for the  $\cos \psi_0$  scale factor on the wavenumber components, this is precisely the same as for the 2-D case, and can be processed the same as well.

The bottom line is that the projection allows us to pretend we have a 2 dimensional problem and form an image accordingly. The specialized data collection presumptions of this section would require the interpolation of the projected data to a Cartesian grid for efficient transformation using a 2-D FFT.

## 4.2 Generalized Data Collection with Real-time Motion Compensation

Without the limitations of the prior section, the more general model for the collected phase history data is

$$X_V(i, n) \approx A_R \sigma(\mathbf{s}) \exp j \{ k_x(i, n) s_x + k_y(i, n) s_y + k_z(i, n) s_z \}, \quad (121)$$

where

$$\begin{aligned} k_x(i, n) &= k(i) \cos \psi_n \sin \alpha_n = \frac{2}{c} [\omega_n + \gamma_n T_{s, n} i] \cos \psi_n \sin \alpha_n, \\ k_y(i, n) &= -k(i) \cos \psi_n \cos \alpha_n = -\frac{2}{c} [\omega_n + \gamma_n T_{s, n} i] \cos \psi_n \cos \alpha_n, \text{ and} \\ k_z(i, n) &= k(i) \sin \psi_n = \frac{2}{c} [\omega_n + \gamma_n T_{s, n} i] \sin \psi_n. \end{aligned} \quad (122)$$

The actual flight path, whatever it is, will stipulate how  $\psi_n$  varies with  $\alpha_n$ .

Since we are interested in the projection of the data to  $k_z = 0$ , we are mostly interested in getting an ultimate phase history data set on the right  $(k_x, k_y)$  grid, whether by interpolation, or by motion compensation. We will presume to do as much with motion compensation as possible.

### Motion Compensation

As with the 2-D case, we first want  $k_y(i, n)$  to not vary with pulse index  $n$ . That is, we want

$$k_y(i, n) = k_y(i, 0) = k_y(i). \quad (123)$$

This implies that we want

$$[\omega_n + \gamma_n T_{s, n} i] \cos \psi_n \cos \alpha_n = [\omega_0 + \gamma_0 T_{s, 0} i] \cos \psi_0. \quad (124)$$

This is achieved if we adjust

$$[\omega_n + \gamma_n T_{s, n} i] = [\omega_0 + \gamma_0 T_{s, 0} i] \left( \frac{\cos \psi_0}{\cos \psi_n \cos \alpha_n} \right), \quad (125)$$

which can be accomplished by

$$\omega_n = \omega_0 \left( \frac{\cos \psi_0}{\cos \psi_n \cos \alpha_n} \right), \text{ and } \gamma_n = \gamma_0 \left( \frac{\cos \psi_0}{\cos \psi_n \cos \alpha_n} \right), \quad (126)$$

with  $T_{s,n} = T_{s,0}$ .

This defines the radial wavenumber distance as

$$k(i) = \frac{2}{c} [\omega_n + \gamma_n T_{s,n} i] = \frac{2}{c} [\omega_0 + \gamma_0 T_{s,0} i] \left( \frac{\cos \psi_0}{\cos \psi_n \cos \alpha_n} \right). \quad (127)$$

Also as with the 2-D case, a linear spacing of the Fourier domain samples in the  $k_x$  direction is achieved by setting

$$\begin{aligned} k_x(i, n) &= k(i) \cos \psi_n \sin \alpha_n = \frac{2}{c} [\omega_0 + \gamma_0 T_{s,0} i] \cos \psi_0 \tan \alpha_n \\ &= \frac{2}{c} [\omega_0 + \gamma_0 T_{s,0} i] \cos \psi_0 d\alpha n. \end{aligned} \quad (128)$$

That is, we choose sampling positions along the synthetic aperture where

$$\tan \alpha_n = d\alpha n. \quad (129)$$

Data collected in the manner just described is modeled by

$$X_V(i, n) \approx A_R \sigma(\mathbf{s}) \exp j \{ k_x(i, n) s_x + k_y(i) s_y + k_z(i, n) s_z \}, \quad (130)$$

where

$$\begin{aligned} k_x(i, n) &= \frac{2}{c} [\omega_0 + \gamma_0 T_{s,0} i] \cos \psi_0 d\alpha n, \\ k_y(i) &= -\frac{2}{c} [\omega_0 + \gamma_0 T_{s,0} i] \cos \psi_0, \text{ and} \\ k_z(i, n) &= \frac{2}{c} [\omega_0 + \gamma_0 T_{s,0} i] \left( \frac{\cos \psi_0}{\cos \psi_n} \right) \tan \psi_n. \end{aligned} \quad (131)$$

Remember that the presumption that  $s_z = 0$  renders  $k_z(i, n)$  inconsequential.

Data collected in this manner will always project to a trapezoidal grid suitable for processing with a CZT. Figure 11 illustrates a broadside data collection, and figure 12 illustrates a severely squinted data collection. Figure 13 illustrates a sinusoidal porpoising broadside flight path, and figure 14 illustrates a sinusoidal porpoising severely squinted

flight path. All have identical projections onto the  $k_z = 0$  plane, and can be processed identically via the CZT.

Data collected in this manner substantially simplifies image formation for squinted collection geometries.<sup>9</sup>

### 4.3 Image Formation using CZT

Let us now return to the model for the motion compensated phase history data, but with the presumption that  $s_z = 0$ , namely

$$X_V(i, n) \approx A_R \sigma(\mathbf{s}) \exp j \{ k_x(i, n) s_x + k_y(i) s_y \}, \quad (132)$$

where

$$\begin{aligned} k_x(i, n) &= \frac{2}{c} [\omega_0 + \gamma_0 T_{s,0} i] \cos \psi_0 d \alpha n, \text{ and} \\ k_y(i) &= -\frac{2}{c} [\omega_0 + \gamma_0 T_{s,0} i] \cos \psi_0. \end{aligned} \quad (133)$$

We rewrite the data as

$$X_V(i, n) \approx [A_R \sigma(\mathbf{s}) \exp j \{ k_y(i) s_y \}] \exp j \{ k_x(i, n) s_x \}, \quad (134)$$

and expand it as

$$X_V(i, n) \approx [A_R \sigma(\mathbf{s}) \exp j \{ k_y(i) s_y \}] \exp j \left\{ \frac{2\omega_0 \cos \psi_0}{c} d \alpha s_x \left( 1 + \frac{\gamma_0 T_{s,0}}{\omega_0} i \right) n \right\}. \quad (135)$$

The first transform will be an azimuth transform across index  $n$ . Consequently, the items in the square brackets are constants as far as the transform is concerned.

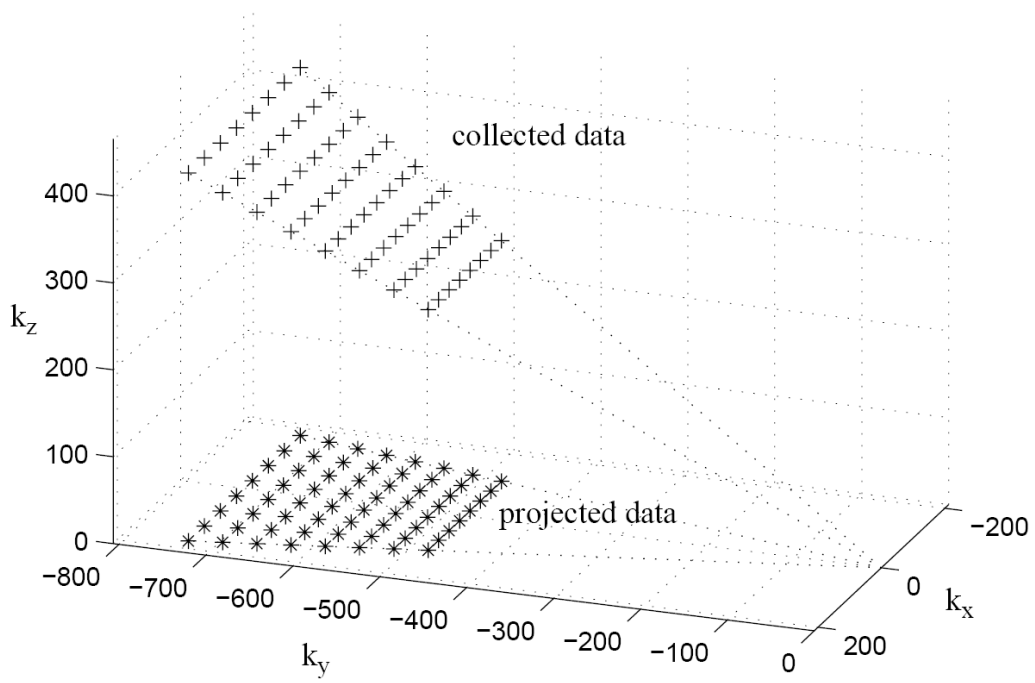


**Figure 11. Fourier space locations of motion compensated phase history data from broadside straight-line flight geometry.**

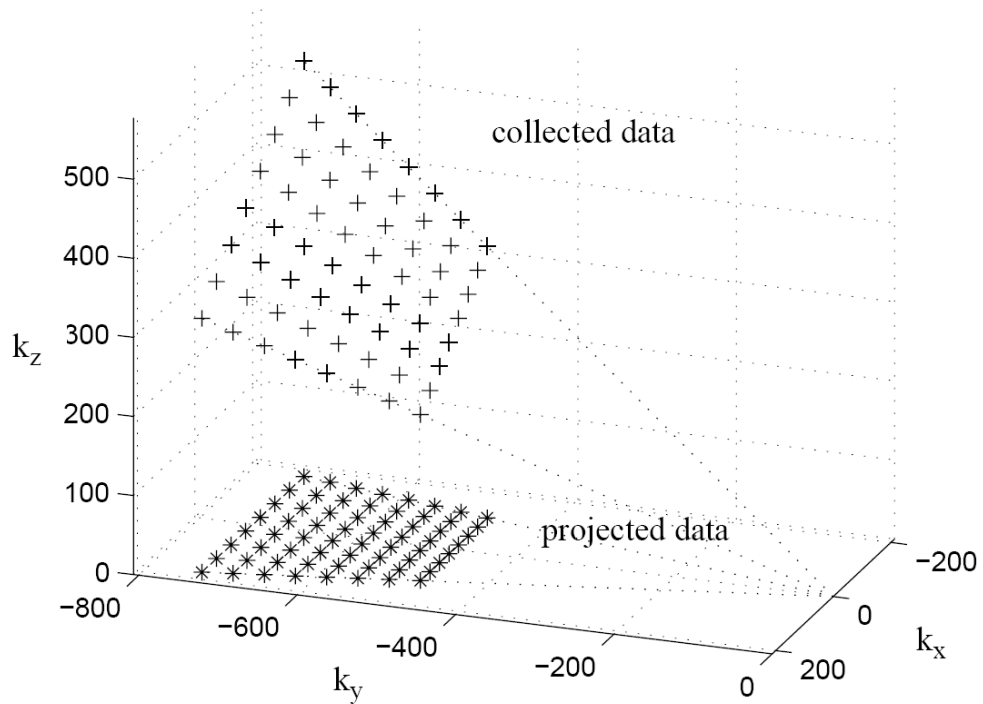


**Figure 12. Fourier space locations of motion compensated phase history data from squinted straight-line flight geometry.**

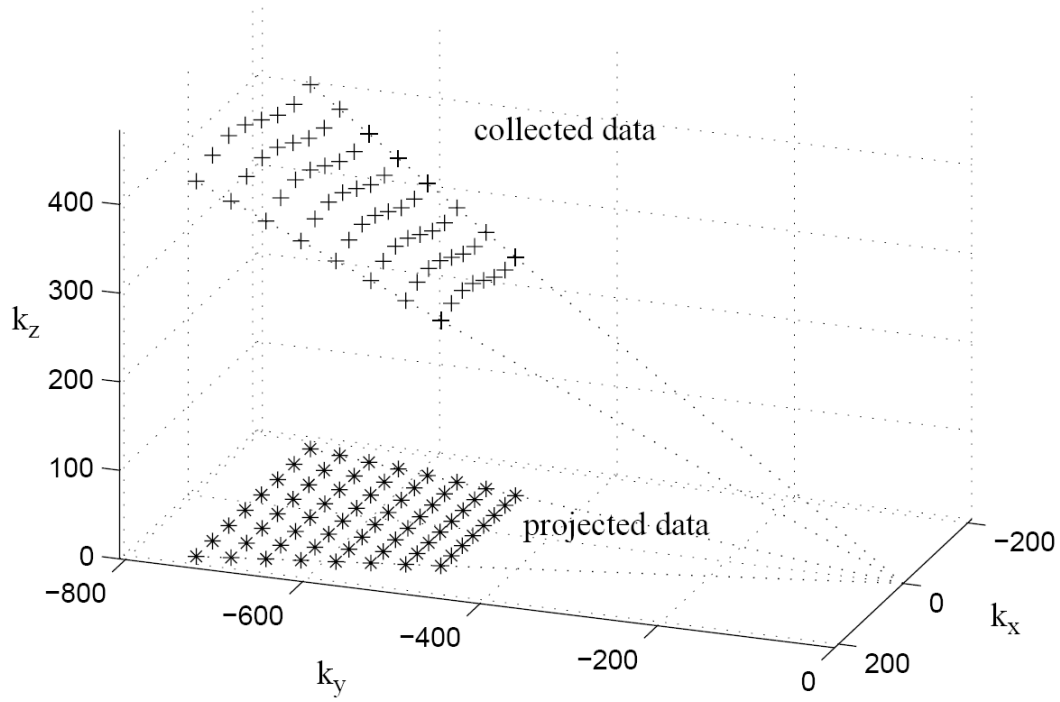


**Figure 13. Fourier space locations of motion compensated phase history data from broadside porpoising flight geometry.**

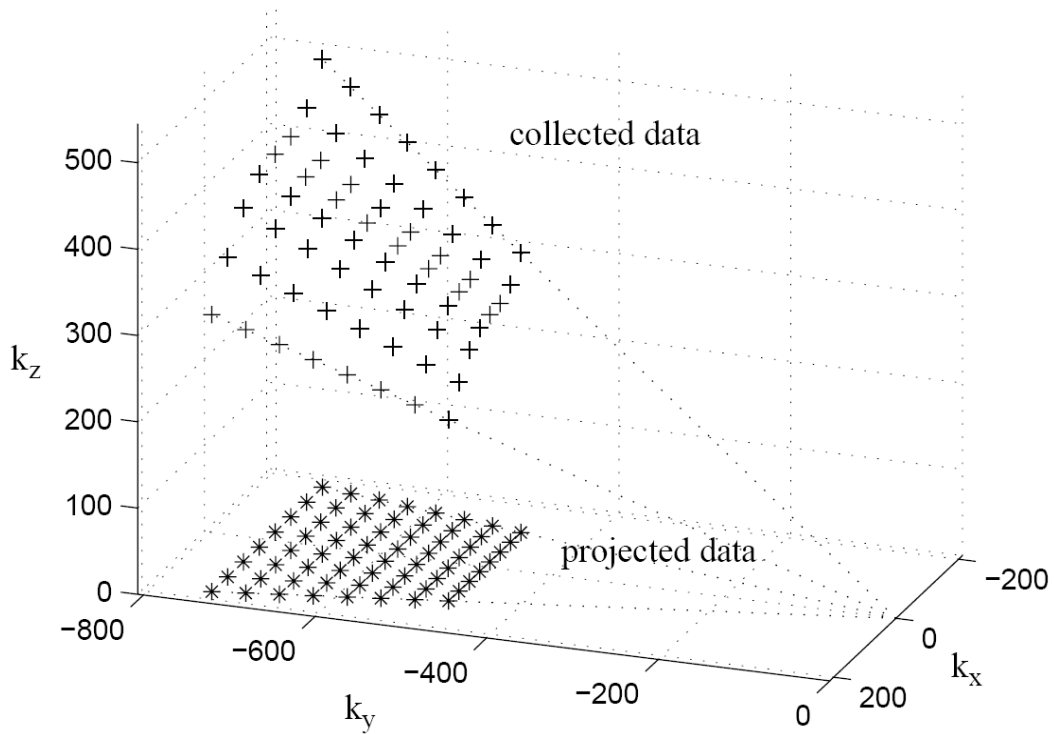


**Figure 14. Fourier space locations of motion compensated phase history data from squinted porpoising flight geometry.**

Azimuth Processing using CZT

Now consider an application of the CZT directly to equation (135), where

$$\begin{aligned}
 CZT_n\{X_V(i, n)\} &\approx [A_R\sigma(\mathbf{s})\exp j\{k_y(i)s_y\}]\sum_n \left( e^{j\left\{\frac{2\omega_0 \cos\psi_0}{c}d\alpha s_x\left(1+\frac{\gamma_0 T_{s,0}}{\omega_0}i\right)n\right\}} \right) e^{-j\Delta_f u n} \\
 &\approx [A_R\sigma(\mathbf{s})\exp j\{k_y(i)s_y\}]\sum_n \left( e^{j\left\{\frac{2\omega_0 \cos\psi_0}{c}d\alpha s_x\left(1+\frac{\gamma_0 T_{s,0}}{\omega_0}i\right)-\Delta_f u\right\}n} \right).
 \end{aligned} \tag{136}$$

If we force  $\Delta_f$  to vary with index  $i$ , that is we scale frequency spacing to

$$\Delta_f = \frac{2\pi}{N}\left(1+\frac{\gamma_0 T_{s,0}}{\omega_0}i\right), \tag{137}$$

then we have

$$CZT_n\{X_V(i, n)\} \approx \left[ \begin{array}{l} [A_R\sigma(\mathbf{s})\exp j\{k_y(i)s_y\}] \\ \times \sum_n \left( e^{j\left(1+\frac{\gamma_0 T_{s,0}}{\omega_0}i\right)\left\{\frac{2\omega_0 \cos\psi_0}{c}d\alpha s_x - \frac{2\pi}{N}u\right\}n} \right) \end{array} \right]. \tag{138}$$

Performing the summation yields

$$CZT_n\{X_V(i, n)\} \approx \left[ \begin{array}{l} [A_R\sigma(\mathbf{s})\exp j\{k_y(i)s_y\}] \\ \times W_n\left(\left(1+\frac{\gamma_0 T_{s,0}}{\omega_0}i\right)\left\{\frac{2\omega_0 \cos\psi_0}{c}d\alpha s_x - \frac{2\pi}{N}u\right\}\right) \end{array} \right]. \tag{139}$$

This also clearly offers a peak response when

$$\frac{2\pi}{N}u = \frac{2\omega_0 \cos\psi_0}{c}d\alpha s_x. \tag{140}$$

with location that is independent of index  $i$ .

As with the 2-D case, we again note that the image impulse response (IPR) width will vary slightly as a function of index  $i$ , but the peak location will not.

To complete the image formation, we need to transform across index  $i$ .

### Range Processing with FFT

Consider the results of the azimuth CZT, rearranged here as follows

$$CZT_n\{X_V(i, n)\} \approx \left[ \begin{array}{l} A_R \sigma(\mathbf{s}) W_n \left( \left( 1 + \frac{\gamma_0 T_{s,0}}{\omega_0} i \right) \left\{ \frac{2\omega_0 \cos \psi_0}{c} d\alpha s_x - \frac{2\pi}{N} u \right\} \right) \\ \times \exp j \{ k_y(i) s_y \} \end{array} \right]. \quad (141)$$

Ignoring the slight fluctuation in the width of the azimuth IPR, and expanding  $k_y(i) = -(2/c)[\omega_0 + \gamma_0 T_{s,0} i] \cos \psi_0$  yields

$$CZT_n\{X_V(i, n)\} \approx \left[ \begin{array}{l} A_R \sigma(\mathbf{s}) W_n \left( \frac{2\omega_0 \cos \psi_0}{c} d\alpha s_x - \frac{2\pi}{N} u \right) e^{j \left\{ -\frac{2}{c} \omega_0 \cos \psi_0 s_y \right\}} \\ \times e^{j \left\{ -\frac{2}{c} \gamma_0 T_{s,0} \cos \psi_0 s_y \right\} i} \end{array} \right]. \quad (142)$$

which has phase linear in index  $i$ .

Performing a FFT across index  $i$  yields

$$\begin{aligned} FFT_i\{CZT_n\{X_V(i, n)\}\} &= \sum_i CZT_n\{X_V(i, n)\} e^{-j \frac{2\pi}{I} vi} \\ &\approx \left[ \begin{array}{l} A_R e^{j \left\{ -\frac{2}{c} \omega_0 \cos \psi_0 s_y \right\}} \sigma(\mathbf{s}) W_n \left( \frac{2\omega_0 \cos \psi_0}{c} d\alpha s_x - \frac{2\pi}{N} u \right) \\ \times \sum_i e^{-j \left\{ \frac{2}{c} \gamma_0 T_{s,0} \cos \psi_0 s_y + \frac{2\pi}{I} v \right\} i} \end{array} \right] \\ &\approx A_R e^{j \left\{ -\frac{2}{c} \omega_0 \cos \psi_0 s_y \right\}} \sigma(\mathbf{s}) \left[ \begin{array}{l} W_n \left( \frac{2\omega_0 \cos \psi_0}{c} d\alpha s_x - \frac{2\pi}{N} u \right) \\ \times W_i \left\{ \frac{2}{c} \gamma_0 T_{s,0} \cos \psi_0 s_y + \frac{2\pi}{I} v \right\} \end{array} \right]. \end{aligned} \quad (143)$$

This clearly offers a peak response when

$$\frac{2\pi}{I} v = -\frac{2}{c} \gamma_0 T_{s,0} \cos \psi_0 s_y, \quad (144)$$

as well as when

$$\frac{2\pi}{N} u = \frac{2\omega_0 \cos \psi_0}{c} d\alpha s_x. \quad (145)$$

As before, the residual phase perturbation is inconsequential to a magnitude detected image, but could be compensated if so desired.

Equation (143) represents the 2-D complex IPR of a point target in a 3-D geometry.

Another minor note is that the phase in the residual exponential factor in equation (143) that depends on  $s_y$  does not affect the normally displayed image, so is commonly ignored. However, this term does play a role in the image spectrum.

*“I never said most of the things I said.”*  
*-- Yogi Berra.*

## 5 MATLAB Implementation

The following MATLAB function forms images using the CZT approach to Polar Format processing on data with real-time motion compensation applied as indicated in the previous section of this report. No attempt has been made to optimize this code.

```

%SARPF      sar image formation, polar format processing
%
% cimg = sarpf(data_parms, phistdata)
%
% data_parms = [rc0 psi0 dalpha N w0 g0 Ts0 I rhox rhoy delx dely]
% phistdata = phase history data
%
% cimg = complex image
%
% phistdata is a phase history data array with each row representing a
% deramped range return. Row number denotes azimuth sample number.
%
% cimg is the resulting complex image in [x,y] format, where row
% number equates to x position, and column number denotes y position.

function cimg = sarpf(parms,phistdata)

c = 299.792e6;

%%%%%%%%%%%%%%%%%%%%%%%%%%%%%%%%%%%%%%%%%%%%%%%%%%%%%%%%%%%%%%%%%%%%%%%%
% extract image formation parameters

rc0   = parms(1);      % nominal range to scene center - m
psi0  = parms(2);      % nominal depression angle - rad
dalpha = parms(3);    % nominal increment in tan(aperture_angle)
N      = parms(4);      % number azimuth samples
w0     = parms(5);      % nominal center frequency - rad/sec
g0     = parms(6);      % nominal chirp rate - rad/sec^2
Ts0    = parms(7);      % nominal A/D sample period - sec
I      = parms(8);      % number range samples
rhox   = parms(9);      % desired x resolution
rhoy   = parms(10);     % desired y resolution
delx   = parms(11);     % desired x pixel spacing
dely   = parms(12);     % desired y pixel spacing
Dx     = parms(13);     % desired x scene diameter
Dy     = parms(14);     % desired y scene diameter

[N,I] = size(phistdata); % redefine N,I based on data

cospsi0 = cos(psi0); % cosine of depression angle
lambda  = 2*pi*c/w0; % nominal wavelength

rhox = lambda/(2*N*dalpha*cos(psi0)); % actual resolution
rhoy = 2*pi*c/(2*g0*Ts0*(I-1)*cos(psi0)); % actual resolution

U = min(2*round(Dx/delx/2),2*round(N*rhox/delx/2));
% actual number of x pixels
delx = min(Dx/U,rhox*N/U); % calculate actual delx
os_az = rhox/delx; % x oversample factor
N_ = round(N*os_az);
N__ = max(U,N); % MATLAB required CZT length

```

```

V      = min(2*round(Dy/dely/2),2*round(I*rhoy/dely/2));
                                % actual number of y pixels
I_     = 2*round(I*os_ra/2);    % range FFT length required
I__    = max(V,I);

%%%%%%%%%%%%%%%%%%%%%%%%%%%%%%%%%%%%%%%%%%%%%%%%%%%%%%%%%%%%%%%%%%%%%%%%
% form image
%%%%%%%%%%%%%%%%%%%%%%%%%%%%%%%%%%%%%%%%%%%%%%%%%%%%%%%%%%%%%%%%%%%%%%%%
% azimuth processing

disp(' beginning azimuth processing');

argW = -j*2*pi/(N*os_az);      % calculate nominal CZT parms
argA = -j*pi*U/(N*os_az);

img1 = j*ones(U,I);          % reserve memory block

for i=1:I,
    beta = 1 + (g0*Ts0/w0)*(i-1-I/2);    % calculate freq scale factor

    x = phistdata(:,i);
    y = czt(x,N__,exp(argW*beta),exp(argA*beta)); % perform azimuth CZT
    y = y(1:U);          % cull meaningful data

    %%% perform a phase bias correction resulting from the CZT
    pcorr = (pi-(2*w0*cospsi0/c)*(beta*delx*dalpha*N/2) )*[-U/2:U/2-1];
    img1(:,i) = y .* exp(-j*pcorr);
end

%%%%%%%%%%%%%%%%%%%%%%%%%%%%%%%%%%%%%%%%%%%%%%%%%%%%%%%%%%%%%%%%%%%%%%%%
% range processing

disp(' beginning range processing');

img1 = img1.';          % perform corner turn

cimg = fft( img1,I_ ); % perform range FFT
cimg = cimg((I_/2-V/2+1):(I_/2+V/2),:); % crop range swath

cimg = cimg.';

%%%%%%%%%%%%%%%%%%%%%%%%%%%%%%%%%%%%%%%%%%%%%%%%%%%%%%%%%%%%%%%%%%%%%%%%
return;

```

## 6 Polar Format Processing Extensions

The basic Polar Format image formation algorithm can be extended in a variety of manners, to enhance its capabilities. Several of these are discussed in this section.

### Background

The development of Polar Format processing made several presumptions along the way. These include the presumption of a negligible Residual Video Phase Error term in equation (34), and the plane-wave approximation in equation (115). The error in these presumptions ultimately limits the scene size that is adequately focused. However, several techniques have been developed to significantly mitigate the effects of these errors.

Some of these are briefly discussed here.

### 6.1 Residual Video Phase Error Correction

Equation (34) should really look more like

$$X_V(t) \approx A_R \sigma(\mathbf{s}) \text{rect}\left(\frac{t-t_c}{T}\right) \exp j\left\{\omega(t_c-t_s) + \gamma(t-t_c)(t_c-t_s) + \frac{\gamma}{2}(t_c-t_s)^2\right\}. \quad (146)$$

The final phase term  $(\gamma/2)(t_c-t_s)^2$  is often called the Residual Video Phase Error (RVPE), and is a consequence of stretch processing (deramping or demodulating with a common LO chirp). It can, in some cases, significantly impact the focused scene size achievable.<sup>10</sup> This error term is generally dealt with in one of three possible ways.

- 1) In classical Polar Format processing it is ignored outright.
- 2) In some algorithms (e.g. subaperture techniques) it is approximated and ‘mostly’ removed.
- 3) It can be removed completely by preprocessing the data. This requires for each azimuth sample performing a range DFT followed by a phase error correction followed by a range Inverse-DFT.<sup>11</sup> This process is sometimes called a “deskew” operation.<sup>5</sup>

We note that the RVPE does not exist in stepped-frequency chirps, sometimes called ‘synthetic’ chirps.

## 6.2 Polar Format Processing with Subapertures

The planar wavefront presumption, when we in fact truly have wavefront curvature, leads to phase errors in the data that depend on the spatial position of the target, or scene element. Consequently, the manifestation is ‘spatially-variant’ phase errors. Different parts of the scene exhibit different phase errors, all due to the variability in the wavefront curvature across the scene.

The variations are slowly varying across the scene, which means that a neighborhood of locations exhibit nearly common phase errors. Consequently, neighborhoods can be effectively treated by a common correction or compensation. This allows subaperture techniques to be used to relatively efficiently mitigate the effects of wavefront curvature (and residual video phase errors, too). In fact, subaperture techniques can often be employed to do even somewhat similar things as the polar reformatting itself. However, subaperture techniques on truly polar reformatted data work much better yet.<sup>2</sup>

## 6.3 Partial Wavefront Curvature Error Correction Between Transforms

If Polar Format processing is implemented as an azimuth transform followed by a range transform, then an opportunity exists between the two transforms to mitigate ‘some’ of the effects of wavefront curvature. That is, after the azimuth transform, but prior to the range transform, we have an estimate of the azimuth position of target locations. Consequently, errors that depend on index  $i$  and azimuth location  $s_x$  can be compensated to some degree.

## 6.4 Wavefront Curvature Correction in Post Processing

The spatial variance of the phase errors due to wavefront curvature are deterministic. Consequently they can be compensated by essentially deconvolving the image with the spatially variant response. This means that we know how to filter correctly to sharpen the impulse response at the various locations within the image. It is a post-processing step on the complex image itself and known as Space-Variant Post-Filtering (SVPF).<sup>12,13,14</sup>

## 6.5 Autofocus

Autofocus is likely required at the resolutions where polar reformatting offers significant advantage over other techniques (as resolutions approach the nominal wavelength of the SAR). An algorithm like Phase Gradient Autofocus (PGA) is generally applied after range compression (the range transform).<sup>5</sup> For the CZT/DFT implementation of Polar Format processing, the range transform occurs after the azimuth transform, meaning that autofocus can’t be applied until after the complex image has been formed. That is, the starting place for autofocus is expected to be the formed complex image.

## 6.6 Data Prefiltering

As resolutions approach a wavelength, the polar geometry nature of the collected phase history data is more problematic than wavefront curvature induced spatially variant phase errors. Consequently it is in this realm that Polar Format processing (or its derivatives and extensions) excels in comparison to other techniques.

Since SAR hardware tends to be ‘pixel-limited’ by virtue of finite memory sizes, ultra-fine resolution SAR images tend to be of comparatively small scene spot sizes. For example, a 100-m scene diameter at a 10-km range subtends less than 0.6 degrees, whereas antenna azimuth beamwidths are typically several times wider than that, and can be many tens of times wider than that. A beamwidth of 60 degrees from an L-band antenna would be 100 times as wide as the 100-m spot size at the 10-km range. The radar PRF, however, is determined by the wider antenna azimuth beamwidth. A higher PRF with a finite synthetic aperture length means a larger number of pulses to be collected, and processed. All this suggests that if we can artificially narrow the antenna beam (via signal processing), then we can decimate the data to smaller set, for more efficient processing. We briefly review the design equations here.

Suppose that we have a SAR system with the following parameters

$$\begin{aligned}
 \theta_{az} &= \text{azimuth beamwidth of the antenna,} \\
 k_{a1} &= \text{oversampling factor for the nominal Doppler bandwidth relative to } \theta_{az}, \\
 D_x &= \text{azimuth diameter of the scene of interest, } D_x \ll |\mathbf{r}_c|, \text{ and} \\
 k_{a2} &= \text{new decimated-data oversampling factor relative to } D_x.
 \end{aligned} \tag{147}$$

Now suppose that we wish to filter and decimate the phase history data to a smaller set, more efficiently processed. Then we define the integer decimation factor as

$$d = \frac{k_{a1}}{k_{a2}} \left( \frac{|\mathbf{r}_c| \theta_{az}}{D_x} \right). \tag{148}$$

Prior to decimation, we need to filter the data in azimuth to a fractional bandwidth (two-sided, relative to the azimuth sampling rate of the data) of

$$b_{apf} = \frac{1}{k_{a1}} \left( \frac{D_x}{|\mathbf{r}_c| \theta_{az}} \right). \tag{149}$$

Analysis suggests that for 40 dB stopband rejection, a good rule-of-thumb is for the azimuth prefilter to be an FIR filter with an odd number of weights such that the filter length is

$$N_{apf} \geq 6d - 1. \tag{150}$$

## 6.7 Geometric Corrections

Another aspect of wavefront curvature is geometric errors (distortions) in the image with respect to the actual scene. In the context of earlier discussions, one might consider these as the result of spatially-variant *linear* phase errors.

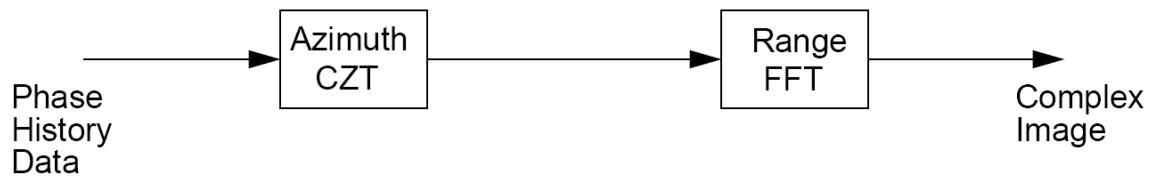
Some geometric distortions (notably horizontal displacements of flat or zero-height targets) can be mitigated via the wavefront curvature corrections cited earlier. Otherwise, these deterministic errors can be corrected in the image by interpolation operations.

Other geometric errors (e.g. those due to target height, such as layover) cannot be corrected without additional information, such as perhaps from a second SAR aperture (e.g. IFSAR).

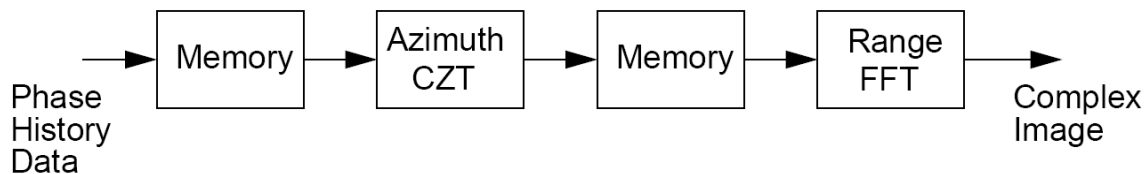
## 7 Block Diagrams

What follows are a series of block diagrams that are increasingly complex in their description of how to implement real-time Polar Format processing. All presume that the phase history data is collected in a manner that places their Fourier-space data projected onto a trapezoidal grid as in Figure 6.

Figure 15 shows the minimal basic processing steps necessary to complete the polar reformatting and to form a complex image of the scene. Implicit in the processing is that the phase history data arrives one pulse at a time, that is, a vector of multiple index  $i$  values arrives prior to a new pulse index  $n$  being incremented. Consequently, the azimuth CZT must wait until an entire synthetic aperture of data is collected, and then first processed across the pulse index  $n$ . If each pulse generates a column of data in the phase history data array, and the CZT and FFT are structured to be column operations, then appropriate data transposes (corner-turn operations) are required. Furthermore, all azimuth CZT operations need to be completed prior to any range FFT operations. Figure 16 adds some detail to the operations by explicitly showing appropriate data collection memories (that may also be considered corner-turn memories). Note that complex image data will be available in 'range-order' unless another corner turning operation is added to the output.



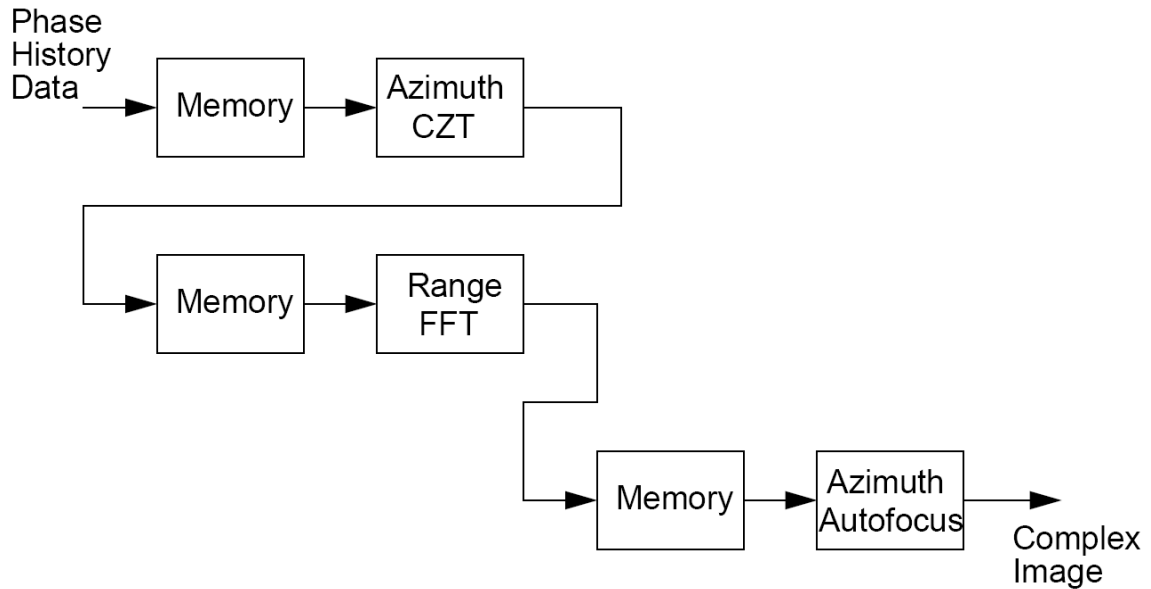
**Figure 15. Minimal transforms required to complete Polar Format processing.**



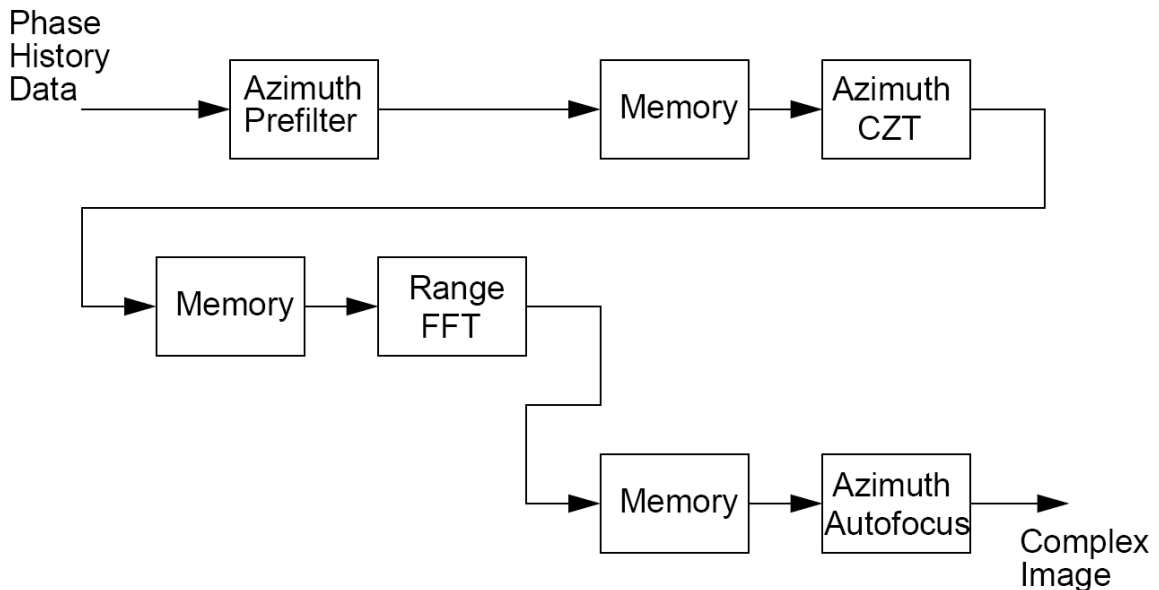
**Figure 16. Minimal transforms required along with data collection (corner turn) memories.**

Figure 17 has added an autofocus operation to the complex image, which is necessarily an azimuth operation. Consequently the complex image output becomes ‘azimuth-order’.

Figure 18 adds an azimuth prefilter, that can begin its operations prior to collecting the entire synthetic aperture’s data.



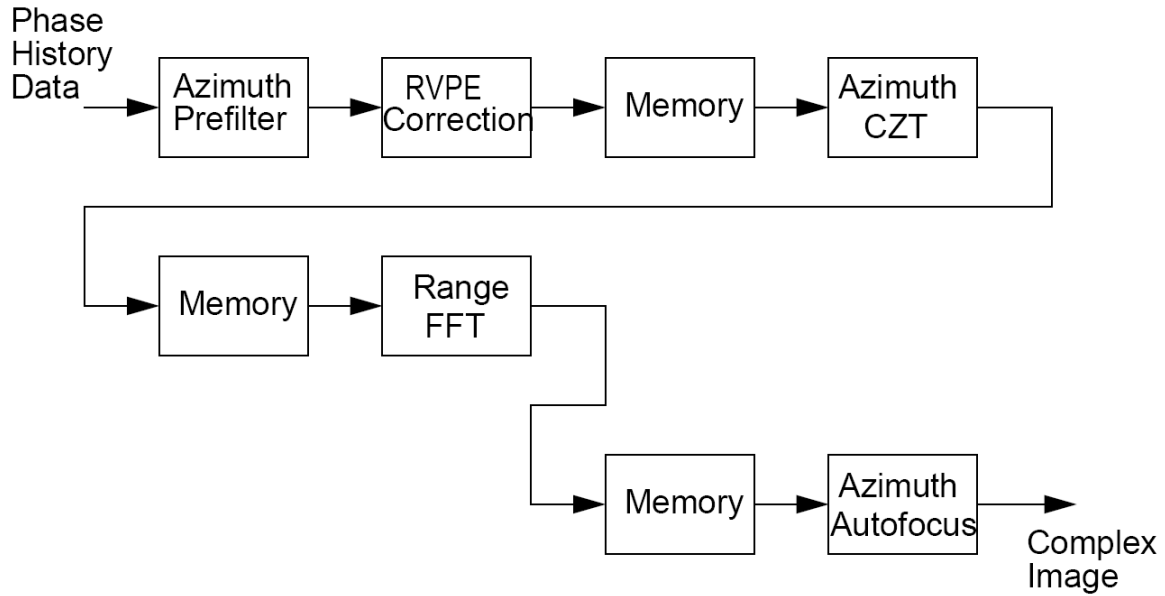
**Figure 17. Polar Format processing with subsequent autofocus operation.**



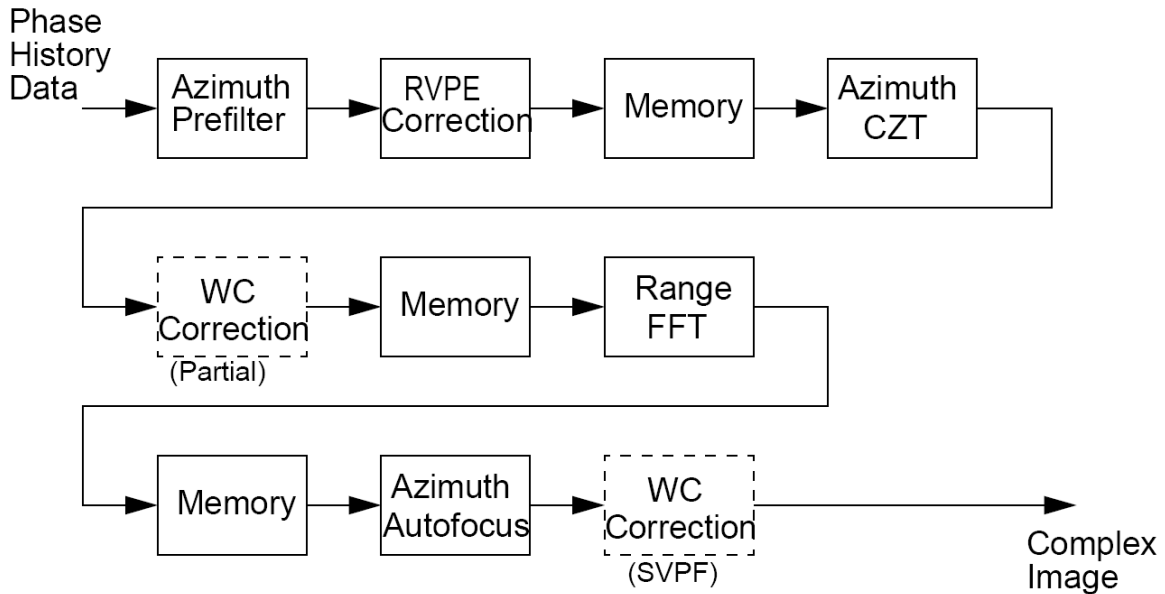
**Figure 18. Polar Format processing with prepended azimuth prefiltering operation.**

Figure 19 incorporates Residual Video Phase Error (RVPE) correction (deskewing).

Figure 20 shows where Wavefront Curvature (WC) corrections can be inserted. These are illustrated with dashed boxes to emphasize that we would never implement both of these at the same time. The partial correction is more efficient, but the SVPF is more complete.



**Figure 19. Polar Format processing with prepended residual video phase error correction.**



**Figure 20. Polar Format processing with wavefront curvature correction.**

Lastly, in Figure 21, geometric correction to the image is added as another post-processing operation that might be applied. In the absence of additional information, this still presumes a flat earth in that it will not correct layover. This box is also dashed to indicate that it is a result of wavefront curvature and may not be required if the SVPF correction is fully implemented.

Clearly, a spectrum of variations exist on basic polar format processing.

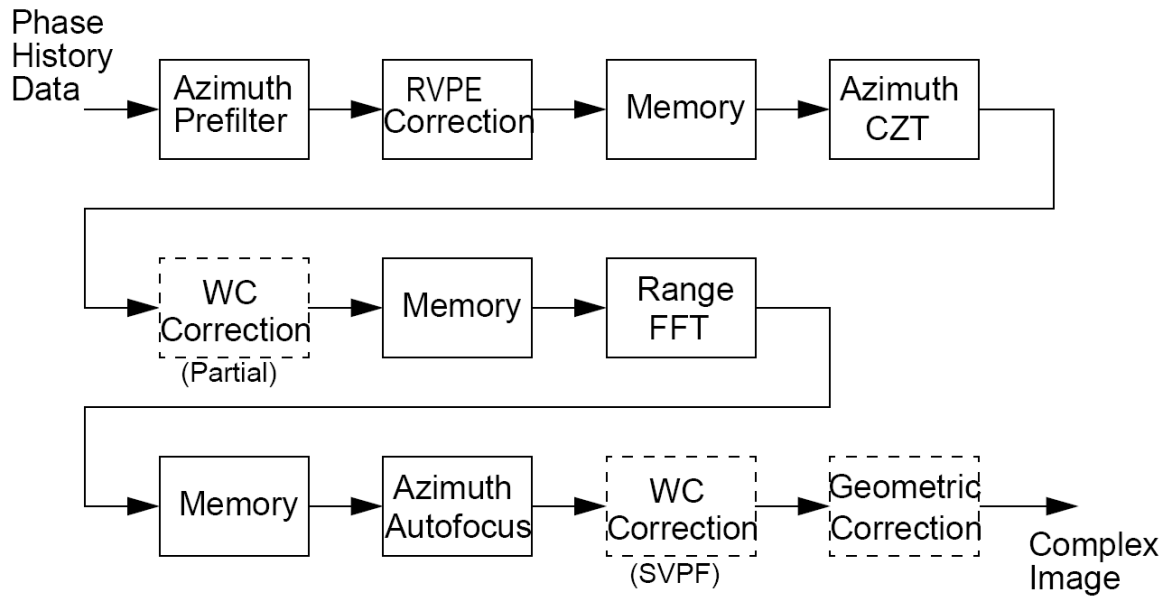


**Figure 21. Polar Format processing with subsequent geometric error correction.**

## 8 Point Design Examples

The following table details two notional SAR systems for which Polar Format processing might be advantageous.

<i>parameter</i>	<i>units</i>	Notional SAR #1	Notional SAR #2
radar band		L/S	Ka
center frequency	GHz	2.45	35
resolution desired	m	0.1016	0.0203
range	m	6389	9260
grazing angle	deg	45.7	19.2
scene azimuth diameter	m	281	41.6
scene range diameter (on ground)	m	211	31.2
antenna nominal azimuth beamwidth	deg	32.4	1.35
aperture angle required	deg	54.1	15.1
number of azimuth samples		63000	19100
number of range (fast-time) samples		2020	2020
azimuth decimation factor supported		12	5

*“Moderation is a virtue only in those who are thought to have an alternative.”*  
*-- Henry A. Kissinger.*

## 9 Conclusions

We observe the following.

- Polar Format (PFA) processing is mainly about recognizing that the SAR phase history data, when de-ramped, represents data in the Fourier space of the scene being imaged. Furthermore, PFA processing is about recognizing that the data from a 3-D scene is collected in a polar (spherical, really) geometry. Furthermore yet, PFA processing is about recognizing the need to get to a Cartesian data location array for efficient processing.
- The polar reformatting required to implement PFA processing can be substantially assisted by proper real-time motion compensation, that is, proper adjustment of radar parameters such that the data is collected whereby it projects to a trapezoidal region in the  $k_z = 0$  plane. This eliminates the traditional range interpolation step of the two-step data resampling algorithm.
- If, additionally, radar pulses are generated at equal increments of  $\tan(a_n)$ , then the azimuth resampling and transform can be combined into a Chirped Z-Transform, dismissing the need for any overt resampling or interpolation steps. The efficiency of implementing a CZT versus resampling followed by a FFT is not addressed.
- Overall processing efficiency might be increased by artificially reducing the antenna beamwidth via an azimuth prefiltering operation prior to any PFA processing.
- A number of additional extensions exist to enhance PFA processing.

The topic of relative merits of Polar Format processing versus other image formation algorithms is not addressed in this report, but is extensively analyzed and treated in a number of other reports and publications. The results render as 'easily defensible' the choice of Polar Format processing (and derivative techniques) for cases where resolution approaches the nominal wavelength of the radar.

*“The superfluous, a very necessary thing.”*  
*-- Voltaire.*

## References

---

- <sup>1</sup> Jack L. Walker, "Range-Doppler Imaging of Rotating Objects", *IEEE Transactions on Aerospace and Electronic Systems*, Vol. AES-16, No. 1, January 1980, pp 23-51.
- <sup>2</sup> Armin W. Doerry, "Synthetic Aperture Radar Processing with Tiered Subapertures", Ph.D. Dissertation, University of New Mexico, May 1995.
- <sup>3</sup> Charles V. Jakowatz, Jr., Daniel E. Wahl, David A. Yocky, Brian K. Bray, Wallace J. Bow, Jr., John A. Richards, "Comparison of algorithms for use in real-time spotlight-mode SAR image formation", SPIE Defense & Security Symposium 2004, Algorithms for Synthetic Aperture Radar Imagery XI, Orlando (Kissimmee), FL, USA, Vol. 5427, 12-16 April 2004.
- <sup>4</sup> Charles V. Jakowatz, Jr., Neall Doren, "Comparison of polar formatting and back-projection algorithms for spotlight-mode SAR image formation", SPIE Defense & Security Symposium 2006, Algorithms for Synthetic Aperture Radar Imagery XIII, Orlando (Kissimmee), FL, USA, Vol. 6237, 17-21 April 2006.
- <sup>5</sup> Charles V. Jakowatz, Jr., Daniel E. Wahl, Paul H. Eichel, Dennis C. Ghiglia, Paul A. Thompson, *Spotlight-mode Synthetic Aperture Radar: A Signal Processing Approach*, ISBN 0-7923-9677-4, Kluwer Academic Publishers, 1996.
- <sup>6</sup> Fred M. Dickey, "Coherent Optical Simulation of Radar Imagery", *Optical Engineering*, Vol. 15 No. 5, September-October 1976.
- <sup>7</sup> Alan V. Oppenheim, Ronald W. Schaffer, *Digital Signal Processing*, ISBN 0-13-214635-5, Prentice-Hall, Inc., Englewood Cliffs, New Jersey, 1975.
- <sup>8</sup> A. W. Doerry, E. Bishop, J. Miller, V. Horndt, D. Small, "Designing interpolation kernels for SAR data resampling", SPIE Defense, Security & Sensing Symposium 2012, Radar Sensor Technology XVI, Baltimore Convention Center, Baltimore, Maryland, USA, Vol. 8361, 23-27 April 2012.
- <sup>9</sup> Armin W. Doerry, "Bandwidth requirements for fine resolution squinted SAR", SPIE 2000 International Symposium on Aerospace/Defense Sensing, Simulation, and Controls, Radar Sensor Technology V, Vol. 4033, Orlando FL, 27 April 2000.
- <sup>10</sup> Armin W. Doerry, "Patch Diameter Limitations due to High Chirp Rates in Focused Synthetic Aperture Radar Images", *IEEE Transactions on Aerospace and Electronic Systems*, Vol. AES-30, No. 4, pp 1125-1129, October 1994.
- <sup>11</sup> Walter G. Carrara, Ron S. Goodman, Ronald M. Majewski, *Spotlight Synthetic Aperture Radar, Signal Processing Algorithms*, ISBN 0-89006-728-7, Artech House, 1995.
- <sup>12</sup> Neall E. Doren, "Space-Variant Post-Filtering for Wavefront Curvature Correction in Polar-Formatted Spotlight-Mode SAR Imagery", Sandia Report SAND99-2706, October 1999.
- <sup>13</sup> Armin W. Doerry, "Wavefront Curvature Limitations and Compensation to Polar Format Processing for Synthetic Aperture Radar Images", Sandia Report SAND2007-0046, Unlimited Release, January 2007.
- <sup>14</sup> Robert Linnehan, Mark Yasuda, Armin Doerry, "An Efficient Means to Mitigate Wavefront Curvature Effects in Polar Format Processed SAR Imagery", SPIE Defense, Security & Sensing Symposium 2012, Radar Sensor Technology XVI, Baltimore Convention Center, Baltimore, Maryland, USA, Vol. 8361, 23-27 April 2012.

## Distribution

Unlimited Release

1	MS 0532	J. J. Hudgens	5240	
1	MS 0519	J. A. Ruffner	5349	
1	MS 0519	A. W. Doerry	5349	
1	MS 0519	L. Klein	5349	
1	MS 0899	Technical Library	9536	(electronic copy)

;-)